J. Mech. Phys. Solids 169 (2022) 105062

Contents lists available at ScienceDirect

Journal of the Mechanics and Physics of Solids

journal homepage: www.elsevier.com/locate/jmps

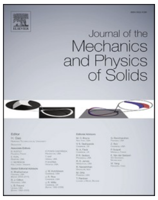

Investigating poromechanical causes for hydraulic fracture complexity using a 3D coupled hydro-mechanical model

Wenfeng Li [a,*], Luke P. Frash [a], Zhou Lei [a], J. William Carey [a], Viet T. Chau [a], Esteban Rougier [a], Meng Meng [a], Satish Karra [a,e], Hoang T. Nguyen [b], Saeed Rahimi-Aghdam [b], Zdeněk P. Bažant [b,c,d], Hari Viswanathan [a]

[a] *Earth and Environmental Sciences, Los Alamos National Laboratory, Los Alamos, NM 87545, United States*
[b] *Department of Civil and Environmental Engineering, Northwestern University, Evanston, IL 60208, United States*
[c] *Department of Mechanical Engineering, Northwestern University, Evanston, IL 60208, United States*
[d] *Department of Materials Science and Engineering, Northwestern University, Evanston, IL 60208, United States*
[e] *Environmental Molecular Sciences Laboratory, Pacific Northwest National Laboratory, Richland, WA, USA*

ARTICLE INFO

Keywords:
Hydraulic fracturing
Biot coefficient
Microplane model
Fracture swarming
HOSS-PFLOTRAN
Parallel cracks

ABSTRACT

Hydraulic fracturing is widely used to increase permeability of tight deep geological formations for improving oil and gas production and enhance geothermal energy extraction. Prior studies often predicted simple planar or near planar hydraulic fractures even though these simple fractures do not adequately explain the measured data. Instead, it is likely that complex fracture networks are created. The phenomenon of hydraulic fracture branching that gives rise to complex fracture networks is poorly understood. In this study, we develop a numerical modeling tool, based on sequential coupling of solid solver HOSS and fluid solver PFLOTRAN, to investigate the mechanisms for hydraulic fracture branching. The spherocylindrical microplane constitutive model is implemented to model fracture growth in anisotropic rocks. We verify our coupled model using the KGD analytical solution. Using a set of simulations, we demonstrate that a hydraulic fracture can branch into lateral directions for certain *in situ* stress conditions if there are pre-existing permeable weak layers whose initial Biot effective stress coefficient is greater than that of the matrix. In addition, we investigate the effect of three-dimensional pre-existing geological discontinuities on the creation of complex fracture systems. Our results demonstrate that branched hydraulic fractures can be predicted if we account for (1) damage-dependent Biot effective stress coefficients and (2) pre-existing geologic discontinuities. This represents a 3D poromechanics mechanism for the creation of branched fracture networks where multiple fractures can propagate simultaneously in a dense parallel swarm.

1. Introduction

Hydraulic fracturing is widely used to stimulate deep low permeability reservoirs for economic oil and gas production. The same technology is also considered for enhancing geothermal systems to create engineered fracture networks for heat extraction. Significant advances have been made in understanding the propagation of a single hydraulic fracture in elastic rock under tectonic stress

---

[*] Corresponding author.
E-mail address: wfli22@outlook.com (W. Li).

https://doi.org/10.1016/j.jmps.2022.105062
Received 26 May 2022; Received in revised form 1 August 2022; Accepted 3 September 2022

(Haimson and Fairhurst, 1967; Detournay, 2004; Bunger et al., 2005; Kanin et al., 2020; Moukhtari et al., 2020; Liu and Lecampion, 2021). Multiple fracture systems have been investigated to study fracture interactions, stability and stress shadow effect (Blanton, 1982; Renshaw and Pollard, 1995; Grassl et al., 2015; Yoon et al., 2015; Gunaydin et al., 2021). Field miscroseismic data and laboratory experiments have shown that hydraulic fractures can simultaneously grow in different directions via crack branching (Zoback et al., 1977; Warpinski and Teufel, 1987; Jeffrey and Settari, 1995; Ishida et al., 2004; Frash et al., 2015; Tan et al., 2017). However, many previous studies failed to predict hydraulic fracture branching, mainly due to insufficient understanding of the key physics of fracture initiation and propagation in heterogeneous subsurface reservoirs.

Past literature presents several mechanisms that can explain fracture branching at the tip of a hydraulic fracture. Zhang et al. (2016) simulated near-wellbore hydraulic fracture branching using fast fluid pressurization rates. Ferguson et al. (2018) also simulated near-wellbore fracture branching by applying mixed-mode shear and tensile rock damage triggered by pressure. Many other studies have based their work on the fracture crossing and arresting criteria proposed by Renshaw & Pollard (1995) to conclude that hydraulic fracture branching favors weak horizontal stress anisotropy and a strong contrast of mechanical properties between pre-existing weak shear-oriented layers and the rock matrix (e.g., Weng et al., 2011; Guo et al., 2018; Cheng et al., 2015). Taleghani (2010) predicted that fracture branches can form in kinked fracture paths when hydraulic cracks intersect weak layers. This kinking-branching mechanism is based on a stress singularity that can enable a hydraulic fracture to continue growing after a weak layer has diverted the fracure. Other models attribute hydraulic fracture branching to heterogeneity (Wu et al., 2009; Manchanda et al., 2020) or extreme injection parameters (Sun et al., 2021). However, none of these prior studies investigated hydraulic fracture branching after a hydraulic fracture has already crossed a pre-existing weak layer, despite this phenomena being observed in nature (Li et al., 2021a). Furthermore, a post-crossing branching behavior could offer an explanation for why branched fractures are so commonly observed in field studies (Warpinski and Teufel, 1987). In this study, we show that this post-crossing branching behavior requires the poromechanical properties of weak layers to change in response to fluid pressure diffusion and that, unlike previous studies, branching can occur without a shear mechanism (Fig. 1). In this study, we define hydraulic fracture branching as a phenomenon that hydraulic fractures simultaneously propagate in multiple directions beyond near-wellbore region. Note that fracture branching is unlike the so-called arresting, crossing, diverting, and offsetting behaviors of hydraulic fractures (Cheng et al., 2015; Kolawole and Ispas, 2020) because branching results in sustainable and simultaneous crack propagation in multiple directions, rather than a change in the direction of a single propagating crack (Li et al., 2021a).

We hypothesize that a time-dependent poromechanical mechanism can cause hydraulic fracture branching in heterogeneous rocks (Fig. 1). After the fluid front in the hydraulic fracture arrives at a pre-existing weak layer, high pressure will diffuse into the weak layer. The excess fluid pressure can then exert sufficient tensile stress on embedded microcrack edges within the weak layer to cause damage. The damage accumulates in the weak layer. We model this damage using an increased local Biot effective stress coefficient. With enough damage (i.e., a Biot coefficient approaching 1.0) the weak layer can reach a tensile stress regime that is sufficient for coalesced fracture propagation. Our hypothesis stems from the physical observation that microcracks are abundant in pre-existing weak layers (Clarkson et al., 2016; Gale et al., 2014). Also, experimental studies have shown that the Biot effective stress coefficient increases as microcracks grow and coalesce in different rock types (Shao, 1998; Hu et al., 2010; Tan et al., 2015). Of particular interest is the work of Hu et al. (2010) who, based on anisotropic poromechanics theory, experimentally proved that the Biot coefficient increases as microcrack damage accumulates in rock samples. Hu's experimental studies were focused on shear fracturing mode, however we expect the damage dependence of the Biot coefficient to also be applicable for tensile fracturing in rocks (Fjaer et al., 2008).

We have implemented our hypothesis of hydraulic fracture branching in a proof-of-concept two-dimensional (2D) numerical model (Chau et al., 2016; Rahimi-Aghdam et al., 2019). This numerical modeling demonstrated that hydraulic fractures can branch at

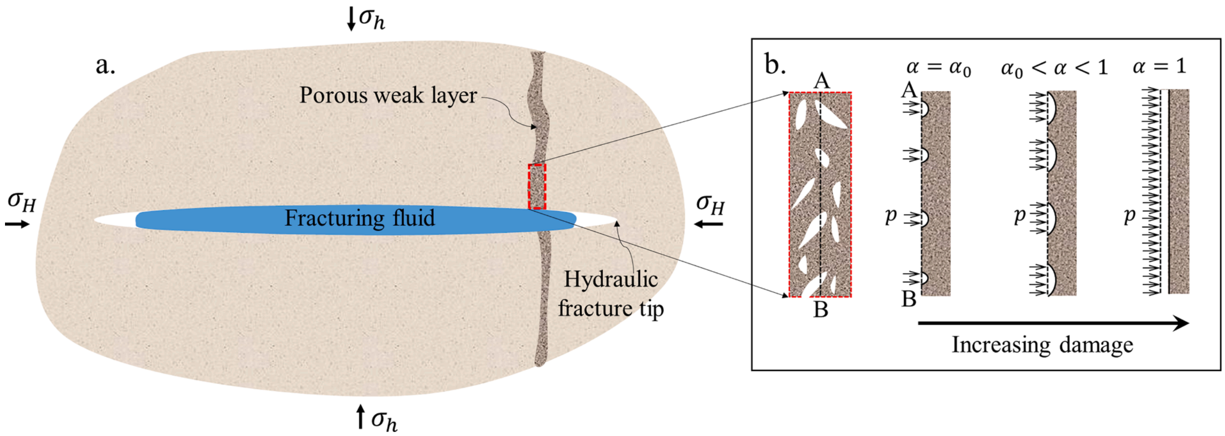

Fig. 1. Hydraulic fracture branching in heterogeneous reservoir. After the hydraulic fracture and fracturing fluid front cross a porous, initially closed weak layer (a), high fluid pressure diffuses into the pores and the microcracks within the weak layer (b). This elevated fluid pressure applies additional stresses onto the microcrack faces, causing damage acculumation (b). This local damage accumulation can increase the Biot effective stress coefficient (Hu et al., 2010), reduce the effective stress normal to the weak layer, and potentially initiate macroscale hydraulic fracture growth along the weak layer.

pre-existing porous weak layers when the Biot coefficient values of the weak layers are related to the microcrack damage accumulation caused by fluid leak-off. It is important to note that the pre-existing weak layers in these models were initially closed and crack branching occurred under anisotropic horizontal stress conditions.

Hydraulic fracture propagation in deep reservoirs is, by nature, a three-dimensional (3D) problem because both hydraulic fractures and geological discontinuities can have complex 3D structures. For example, the existence of stress barriers due to heterogeneity of geological structures can constrain fracture height growth locally (Warpinski and Teufel, 1987; Huang et al., 2019). It is also common for geological discontinuities to exist at different strike and dip angle in the same reservoir (Gale et al., 2014). These geological discontinuities can have non-uniform hydro-mechanical properties across their heights and lengths (Fu et al., 2016). These 3D complexities cannot be simulated using a 2D numerical model. Therefore, it is essential to build a true 3D numerical model for hydraulic fracture branching simulation.

In this study, we present a massively parallel numerical model for 3D hydraulic fracture simulations that can predict branching. Our model couples a finite-discrete element method solid-domain solver with an implicit finite-volume flow and transport solver. We verify the coupling using the classic KGD analytical solution (Geertsma and De Klerk, 1969). We then apply our coupled model to predict hydraulic fracture branching in complex 3D space. We show that, for tight subsurface formations, hydraulic cracks can branch if the Biot coefficients increase as microcracking damage accumulates in weak layers behind the primary fracture tip. This is an additional and separate mechanisms for fracture branching and complexity that what is predicted by fracture tip and fracture interaction theory. Furthermore, we demonstrate that fracture branching can lead to simultaneous growth of multiple parallel cracks.

2. Implementation of microplane model in HOSS for crack analysis

HOSS is a massively parallel simulation platform that is capable of modeling continua using the explicit finite element method (FEM) to solve for displacements and forces in the solid domain (Lei et al., 2014; Knight et al., 2020). More details on the methods used in HOSS can be found in Munjiza (2004). To model fracture propoagation within FEM elements we used the spherocylindrical microplane constitutive model. This simulates the fracturing process within rock via a smeared continuum-element approach. This approach offers several advantages. First, this model is built for continuum elements, so remeshing of the solid domain cracks as they propagate is not required. This significantly reduces computational cost (Bažant and Prat, 1988a and 1988b; Caner and Bažant, 2013). Second, the microplane model enables us to account for plastic deformation, strain-softening, pore dilation, and anisotropic damage in the fracture process zone (Carol and Bažant, 1997). Consideration of these post-failure mechanical characteristics enables us to account for the rock porosity and compressibility changes after failure for effective hydro-mechanical coupling. Note that pore dilation is important for modeling fluid flow and pressure. Third, the microplane model upscales fracture effects to the size of the FEM mesh instead of modeling the fracture geometry directly (Bažant and Planas, 1997). Finally, the microplane model strictly satisfies the tensorial invariance restrictions of stresses and strains when the local principal stresses rotate (Bažant and Ohtsubo, 1977; Bažant and Oh, 1985). In total, this model avoids spurious mesh-size and orientation dependence while preserving a realistic solution at the continuum scale.

In the microplane model, the cracking is smeared over the crack band (element) width with vertical fracture aperture normal to x and y directions as:

$$h_x = l_x \in''_{xx}, \tag{1–1}$$

$$h_y = l_y \in''_{yy}, \tag{1–2}$$

where: h_x and h_y are the crack apertures normal to x and y directions; l_x and l_y are the width of the crack band treated as a scaled quantity to preserve the material fracture energy G_f among various element sizes; and $\in''_{xx}$ and $\in''_{yy}$ are the inelastic parts of the normal strains due to smeared cracking normal to the x and y directions. Horizontal cracks with apertures normal to the z direction are not considered in our model because microseismic data normally reveal vertical hydraulic fractures in unconventional reservoirs (Le Calvez et al., 2007; Maxwell and Cipolla, 2011; Flewelling et al., 2013). Eqs. (1–1) and (1–2) are valid in the present study because we focus on shales whose matrix permeability is on the order of nano-Darcy (Zamirian et al., 2016). As a result, there is only negligible competition between flow in hydraulic cracks and leak-off into adjacent pores. Eqs. (1–1) and (1–2) can be violated when sufficient fluid leak-off at fracture walls is expected for rocks of large matrix permeability owing to the effect of hydraulic fracture propagation regimes. Further, Eqs. (1–1) and (1–2) enable us to regularize the length scale as a function of mesh dimension to preserve the material fracture energy. In a later section, we will perform numerical model verification studies to test the effectiveness of this length scale regularization.

In our model, we consider cracks in orthogonal x and y directions of the global Cartesian coordinate system, as implied by h_x and h_y in Eqs. (1–1) and (1–2). This is inspired by field observations in geological formations in which orthogonal vertical rock joints are often present in geological formations (Gale et al., 2007; Olson, 2004). Hydraulic fracturing can result in one crack system that is perpendicular to the minimum horizontal principal stress σ_h. The second crack system, i.e., the pre-existing weak layers, can occur at angles to the hydraulic fractures, but we shall assume them to be perpendicular to the first crack system so that shear fracture effects can be minimized in our analysis of fracture branching mechanisms. Of course, non-orthogonal crack networks are possible when shear and frictional stresses are transmitted across the crack, but modeling this process brings about a major complication from the solid mechanics viewpoint (Chau et al., 2016). With our inclusion of stress anisotropy, the orthogonal structure can be shown to be a more likely scenario for hydraulic fracture branching.

The crack band widths, l_x and l_y in Eqs. (1–1) and (1–2), are related to the minimum possible spacing of stable parallel cracks (Bažant et al., 1979, 2014). In our model, l_x and l_y are equal to the element dimensions in x and y directions, respectively. It is important to note that l_x and l_y are different from Irwin's material length (the idealized length of the zone of plastic deformation at the crack tip), as implied by the cohesive crack model (Chau et al., 2016).

The inelastic parts of normal strains, ϵ''_{xx} and ϵ''_{yy} in Eqs. (1–1) and (1–2), are computed as:

$$\epsilon''_{ij} = \epsilon_{ij} - \epsilon^{el}_{ij}, \tag{2–1}$$

$$\epsilon^{el}_{ij} = C_{ijkl}\sigma_{kl}, \tag{2–2}$$

where ϵ_{ij} is the strain tensor in the solid element, ϵ^{el}_{ij} is the elastic strain tensor, C_{ijkl} is the transversely isotropic elastic compliance tensor, and σ_{kl} is the stress tensor.

The tensile strength (or loss of cohesion) is governed by Biot's effective stress when fluid pressure is introduced in the porous solid. According to this law, the effective stresses in the solid rock matrix are:

$$S_{ij} = \sigma_{ij} - \delta_{ij}\alpha_0 p, \tag{3}$$

where S_{ij} is the total stress tensor (compressive stress being negative), σ_{ij} is the effective stress, δ_{ij} is the Kronecker delta, α_0 is the initial Biot stress coefficient, and p is the fluid pressure.

The initial Biot stress coefficient of shales can vary between 0.2 and 0.7, depending on the mineral contents and stress states (Ortega et al., 2007; He et al., 2016). Prior experimental studies indicate that this Biot coefficient increases as the cracking damage accumulates and its value depends on the loading direction (Hu et al., 2010; Tan et al., 2015). Therefore, it is fundamentally necessary to generalize the Biot stress coefficient as a tensor, α_{ij}. We must also account for the fact that Biot coefficient terms in the direction perpendicular to the crack propagation evolve from an initial value to 1 as cracking accumulates. For these objectives, the following tensorial form of Biot stress coefficients α_{ij} has been proposed (Rahimi-Aghdam et al., 2019), to match the experimental observations:

$$\alpha_{ij} = \min\left\{\alpha_0\delta_{ij} + \beta\epsilon''_{ij}\left(\epsilon''_{kk}/3\right)^{2/3},\ 1\right\},\ \left(\alpha_0\delta_{ij} < \alpha_{ij} \le 1\right) \tag{4}$$

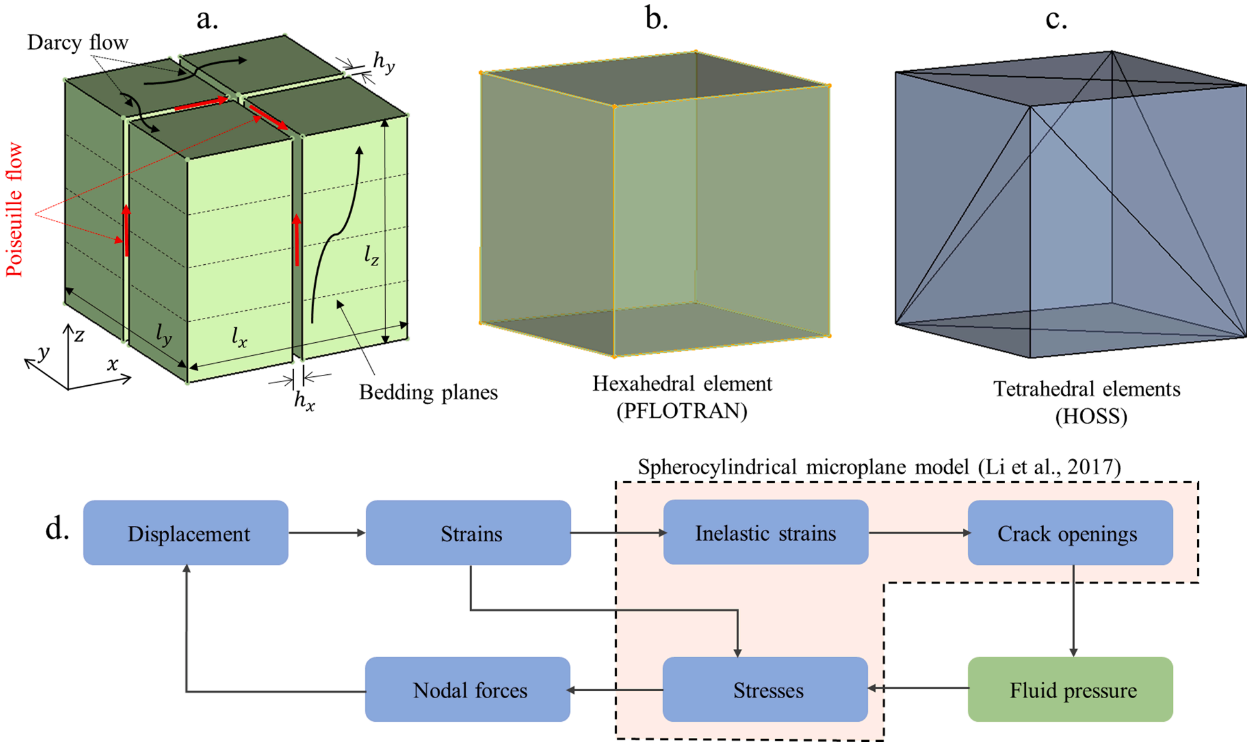

Fig. 2. Representation of fluid flow simulation and the HOSS-PFLOTRAN coupling scheme. Equivalent permeability tensors of a hexahedral element with embedded hydraulic cracks are implicitly implemented in PFLOTRAN (a). PLFOTRAN uses hexahedral elements (b), each of which is divided into six tetrahedrons for meshing in HOSS (c). HOSS solves the mechanical displacements in solid domain (blue in d), while PFLOTRAN solves the fluid pressures (green in d). The spherocylindrical microplane constitutive model (Li et al., 2017) is used to calculate crack openings in the solid domain (dashed lines in d).

In Eq. (4), β is an empirical parameter that links the cracking damage to the Biot stress coefficients. $\in''_{kk}/3\ (=\in''_V)$ is the inelastic relative volumetric expansion.

3. PFLOTRAN for flow in fractured porous media

We use PFLOTRAN to solve the fluid flow in fractured porous rocks. PFLOTRAN is an open-source, massively parallel code that solves multiphase flow and reactive multicomponent transport problems in three-dimensional space (Lichtner et al., 2015). In PFLOTRAN, we mesh the fluid flow domain using hexahedral elements. Depending on the local stress states obtained in HOSS (Knight et al., 2020), the hexahedral elements in PFLOTRAN could contain hydraulic cracks in direction x or y, or both. We use equivalent permeability tensors to implicitly incorporate hydraulic cracks in the hexahedral elements. Fig. 2a illustrates the concept. For the hexahedral element containing hydraulic fractures, fluid flow within the hydraulic cracks and diffusion in the porous rock matrix are both considered.

In hydraulic fractures, fluid flow is assumed to follow the Reynolds equation of classical lubrication theory, i.e., the Poiseuille's law for viscous flow. Based on the cubic law (Witherspoon et al., 1980), fracture permeability is related to the aperture as:

$$\begin{cases} k_x^f = \dfrac{h_y^2}{12}, \\ k_y^f = \dfrac{h_x^2}{12}, \\ k_z^f = \dfrac{h_x^2 + h_y^2}{12}, \end{cases} \tag{5}$$

where k_x^f, k_y^f, and k_z^f are the crack permeability in x, y, and z directions, respectively. This is a simplified approach of modeling fracture flow but it provides a reasonable representation of crack transmissivity at the scale of meters or larger. Studies have shown the deviation of crack permeability from the classic cubic law, especially at microscale, due to fracture roughness (Welch et al., 2021). However, incorporating this consideration brings significant challenges on the meter- or kilometer-scale simulation of hydraulic fracturing. Therefore, we sacrifice the fine-scale characteristics of fracture flow for the sake of technical feasibility of large-scale hydraulic fracturing simulation. Further, in the case of two orthogonal vertical cracks in the same element, k_z^f in Eq. (5) introduces an error due to overlap of the orthogonal fractures. But this error can be shown to be less than 1% for the element sizes of 100 mm and crack apertures of 1 mm in our model.

We use Darcy's law to calculate fluid flow through the pore space of rocks. The intrinsic permeabilities of rock matrix in x, y, and z directions are k_x^m, k_y^m, and k_z^m, respectively. This study focuses on horizontally bedded shales. Thus we assume $k_x^m = k_y^m$, i.e., transversely isotropic permeability, which is supported by laboratory observations on various shales (Pan et al., 2015; Mokhtari and Tutuncu, 2015; Soeder, 1988).

We derive the equivalent permeability of the hexahedral elements by combining fracture permeability and the intrinsic permeability of the rock matrix, as shown in Eq. (6). In the hexahedral elements that are hydraulically fractured, we also allow the fracturing fluid to diffuse, in a transient manner, into the surrounding rock matrix. This fluid leak-off plays a major role in fracture branching (Rahimi-Aghdam et al., 2019; Li et al., 2021a and 2021b). Eq. (6) is valid in this study because hydraulic fractures are all aligned along the global coordinate system. For arbitrarily oriented fractures, complete permeability tensors have been developed (Chen et al., 1999; Lei et al., 2015; Tarahhom et al., 2009).

$$\begin{cases} k_x = k_x^f \dfrac{h_y}{l_y} + k_x^m \left(\dfrac{l_y - h_y}{l_y} \right), \\ k_y = k_y^f \dfrac{h_x}{l_x} + k_y^m \left(\dfrac{l_x - h_x}{l_x} \right), \\ k_z = k_z^f \left(\dfrac{l_y h_x + l_x h_y}{l_x l_y} \right) + k_z^m \left[\dfrac{(l_x - h_x)(l_y - h_y)}{l_x l_y} \right]. \end{cases} \tag{6}$$

4. Hydro-mechanical HOSS-PFLOTRAN coupling

We couple HOSS and PFLOTRAN to account for fluid flow in fractured porous rocks, fracture creation in the rock domain, and poroelastic response of the rock matrix. HOSS and PFLOTRAN are coupled via mapping between compatible meshes (Fig. 2b). PFLOTRAN's internal meshing uses hexahedral elements while HOSS utilizes tetrahedral elements. We divide each hexahedral element in PFLOTRAN into six tetrahedral elements for HOSS. HOSS and PFLOTRAN are sequentially coupled and the updates are lagged by a coupling time-step Δt. According to the solid state variables and fluid pressure at time t, HOSS solves the solid-mechanics for nodal displacements and strains at time $(t+\Delta t)$, using the explicit finite element method with a fixed HOSS-internal time-step (3.0×10^{-6} s in the present study). The spherocylindrical microplane constitutive material model, originally developed by Li et al. (2017), is implemented in HOSS to calculate the crack openings according to the inelastic strains at time $(t+\Delta t)$. This microplane model accounts for fractures through continuum damage zones. Thus individual fractures are not directly modeled and less computational complexity is required. The crack openings calculated in each of the six tetrahedral elements contained within each hexahedral element are averaged and sent to PFLOTRAN. Based on the updated crack openings, PFLOTRAN solves nonlinear flow using a fully implicit Newton-Krylov algorithm that gives the pressure values at the center of each hexahedral element, at the time ($t+\Delta t$). The pressure obtained in each hexahedral element is equally distributed to the six tetrahedral elements for HOSS in the next coupling time-step, which is a simple approach to significantly reduce the complexity of the coupling algorithm.

5. Model verification

Extensive studies have been reported in literature to verify the implementation of HOSS (Knight et al., 2020) and PFLOTRAN (Lichtner et al., 2015). Further, the microplane constitutive model has long been successfully applied to simulate the complex mechanical behavior of several materials, including concrete and rocks (Bažant and Oh, 1983 and 1985; Li et al., 2017). Therefore, in this section, we focus only on the verification of the HOSS-PFLOTRAN coupling with the implemented spherocylindrical microplane constitutive model.

We use the classic KGD analytical solution for hydraulic fracturing to validate the HOSS-PFLOTRAN coupling model. In the 2D plane-strain KGD solution (Geertsma and De Klerk, 1969; Valkó and Economides, 1995), the formation is assumed to be homogeneous and isotropic, and is characterized by elastic modulus E and Poisson's ratio ν. When a Newtonian fluid with dynamic viscosity μ is injected at a constant rate q, a bi-wing hydraulic fracture opens with KGD assuming a constant aperture along the vertical axis within the reservoir height, h_f. In other words, hydraulic fractures have a rectangular vertical cross-section and an elliptical horizontal cross-section. No fluid leak-off is considered at hydraulic fracture walls. With these assumptions, the fracture half-length x_f, the maximum fracture aperture w_{max} (at wellbore wall), and the maximum net fluid pressure in the fracture $p_{net,max}$ can be calculated using Eq. (7).

$$\begin{cases} x_f = 0.539\left(\dfrac{q^3E'}{\mu h_f^3}\right)^{1/6} t^{2/3}, \\ w_{max} = 2.36\left(\dfrac{q^3\mu}{E' h_f^3}\right)^{1/6} t^{1/3}, \\ p_{net,max} = 1.09\left(E'^2\mu\right)^{1/3} t^{-1/3}. \end{cases} \tag{7}$$

In Eq. (7), $E'\left(=\frac{E}{1-\nu^2}\right)$ is the plane-strain modulus, q is the injection rate for one-wing of the hydraulic fracture. The maximum net pressure is defined as the difference between the maximum fluid pressure in the crack (at borehole wall) and the far-field compressive stress normal to the hydraulic fracture.

Table 1 lists all the input parameters for the KGD analytical solution. The KGD results are plotted as the solid lines in Figs. 3d, 3e, and 3f. Table 1 also lists the input parameters for HOSS-PFLOTRAN model. The numerical model has a dimension of 2.5 $m \times$ 4.1 $m \times$ 0.1 m (Fig. 3a). In PFLOTRAN, each hexahedral element has a dimension of 0.1 m in x, y, and z directions. All the six boundaries are assigned to have a Neumann boundary condition with zero fluid flux, except at the injection zone where a constant flux of 0.12 m/s is specified at the side $y = 0$ (Fig. 3a). Converted to volumetric rate, a constant injection flux of 0.12 m/s is equivalent to a constant volumetric injection rate of 0.0012 m^3/s because the injection area (0.01 m^2) remains constant in PFLOTRAN. The initial pore pressure is set as 0.1 MPa because our coupled code does not yet support fluid pressures less than or equal to 0 MPa. Larger initial pore pressure could be used, but is unnecessary, given the ultra-low 5 nD matrix permeability. In our HOSS model we applied boundary conditions that are consistent with the KGD model (Fig. 3a). This included zero z-displacement for nodes on the top and bottom of the model (i.e., plane strain). Also, we applied a zero y-displacement boundary along the base of the model where fluid was injected at the midpoint (i.e., a symmetry boundary). The remaining surfaces were all free boundaries (i.e., zero stress) based on linear superposition where the injection pressure represents the net injection pressure (not the absolute pressure). In other words, the fluid pressure in the hydraulic fracture represents the net fluid pressure in our simulations. We use the input parameters for the spherocylindrical microplane model, as calibrated in Li et al. (2017).

Fig. 3 shows the comparison between the simulation results and the KGD solution. We investigate four different coupling time steps

Table 1
Input parameters of HOSS-PFLOTRAN coupling model and the KGD solution.

Parameter	HOSS-PFLOTRAN model	KGD analytical model
Young's modulus E (GPa)	25.0	25.0
Poisson's ratio ν	0.19	0.19
Initial Biot stress coefficient α_0	0.5	–
Injection rate q (m^3/s)	0.0012	0.0012
Fluid viscosity μ (mPa·s)	0.89	0.89
Model thickness h_f (m)	0.1	0.1
Matrix porosity (%)	10.0	–
Matrix permeability, m^2	4.94×10^{-21}	–
Initial pore pressure (MPa)	0.1	–

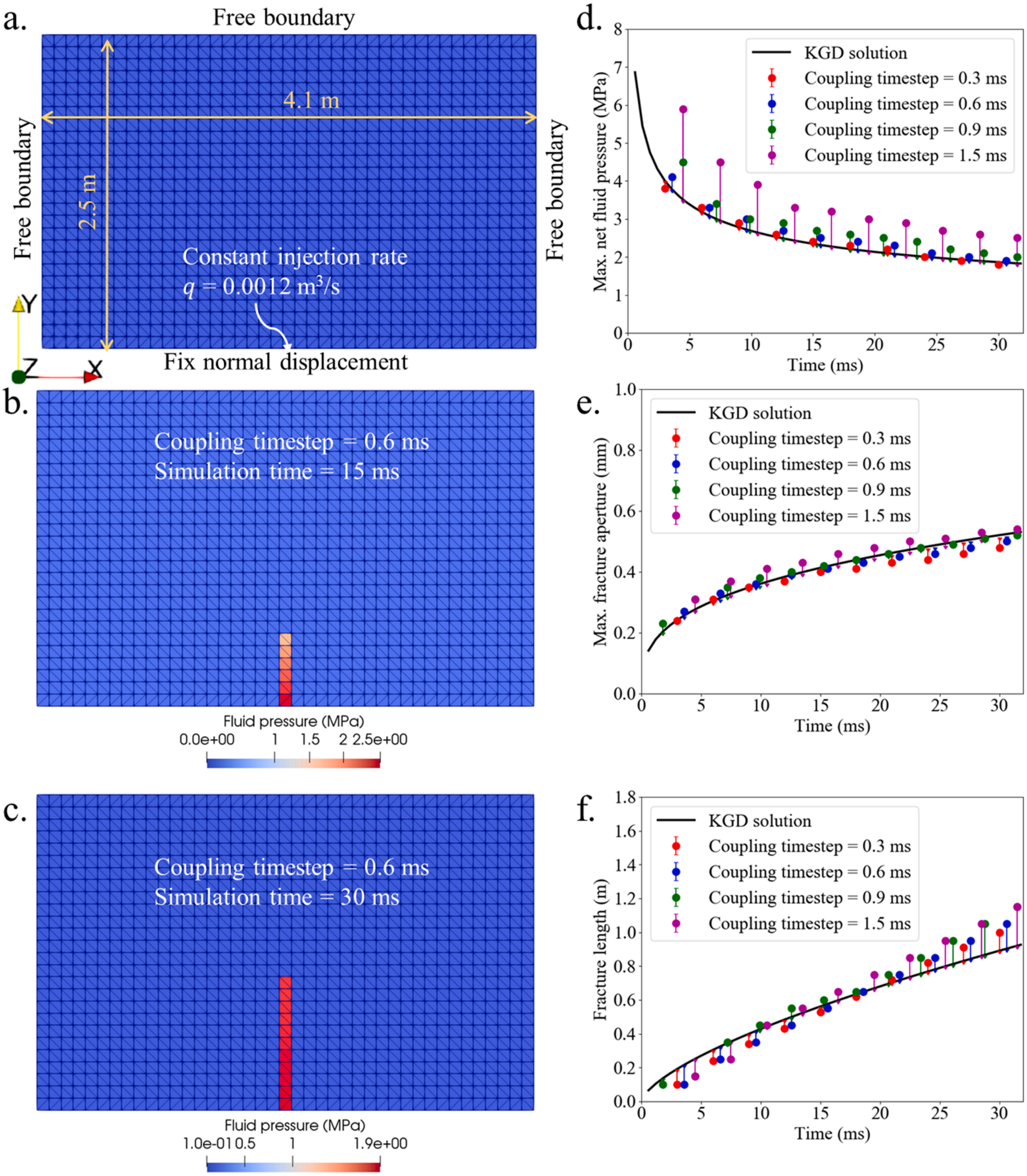

Fig. 3. Validation of HOSS-PFLOTRAN coupling model using KGD analytical solution without fluid leak-off at fracture walls. Plain-strain boundary conditions are assigned to the simulation model to be consistent with KGD model assumptions. Plane of symmetry boundary condition is assigned to the edge that includes the injection point. The simulation results are compared with the KGD analytical solution in terms of the maximum net fluid pressure (d), maximum fracture aperture (e), and fracture length (f) for different coupling time steps. Vertical lines in (d), (e), and (f) are the absolute errors of the simulation results compared with the KGD solution. The net fluid pressure is shown at progressive simulation times when the coupling time step is equal to 0.6 ms (b & c).

in the simulation because improper coupling time steps can cause significant discrepancy between the simulation and the KGD results. To quantify the discrepancy for each coupling time step, we consider all the temporal solutions in Fig. 3 and compute the relative error of the simulation results with respect to the KGD solution, as displayed in Fig. 4. As shown, a coupling time step of 0.6 milli-second (ms)

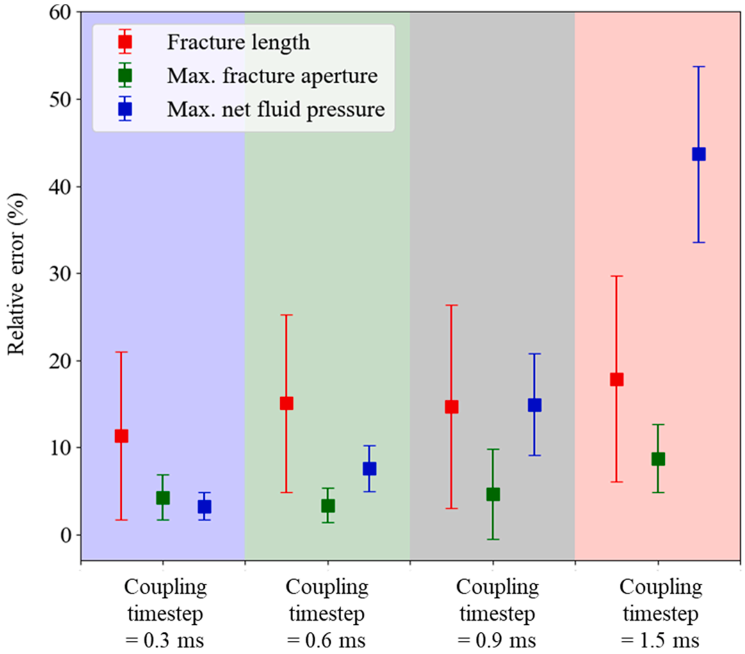

Fig. 4. Relative error of the simulation results compared with the KGD solutions. The square symbol represents the average relative error, whereas the bar represents the standard deviation of the relative error.

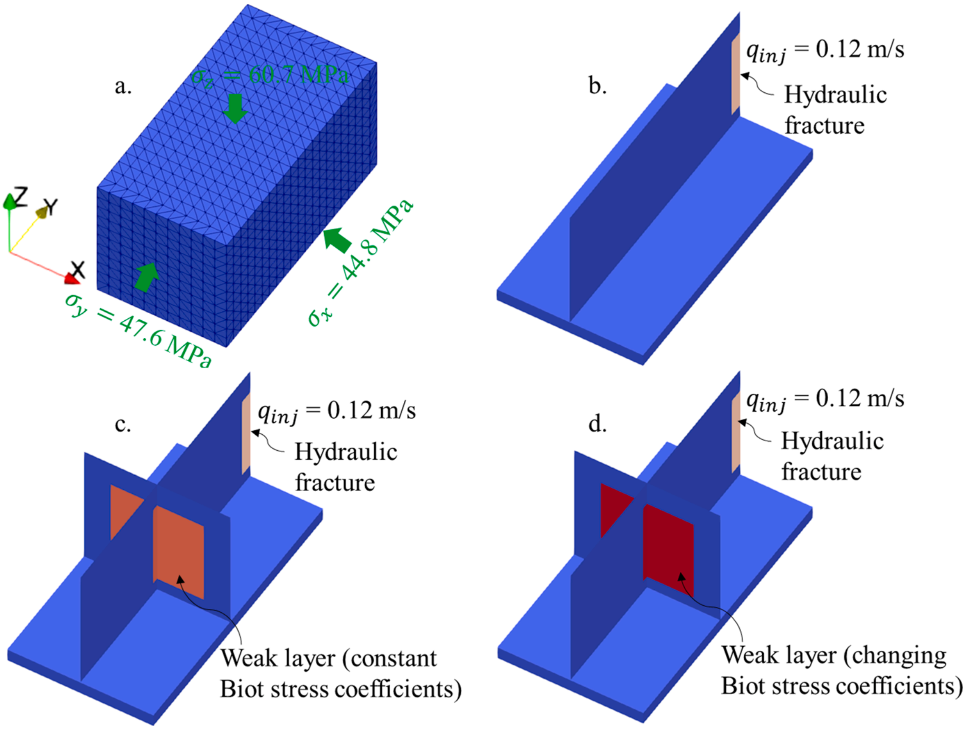

Fig. 5. Three modeling scenarios for demonstration of the hydraulic fracture branching mechanism. (a) shows the model dimension and *in-situ* stresses. There is no pre-existing weak layer in the first modeling scenario (b). In the second scenario (c), a weak layer is defined in the direction perpendicular to the propagation direction of the hydraulic fracture. The weak layer in (c) has a constant Biot stress coefficient in y direction. In the third scenario (d), the tensorial Biot coefficient changes in both of the x and y directions as the inelastic strains accumulate (Eq. (4)).

or less results in small relative errors (nominally <7%) for the maximum fracture aperture and net fluid pressure, but slightly overpredicts the fracture lengths because the microplane model accounts for inelastic strains in the elements ahead of the crack front. For the coupling time steps of 0.9 ms and 1.5 ms, the simulation significantly overpredicts the fracture length and net fluid pressure. Therefore, we use the coupling time step of 0.6 ms in our HOSS-PFLOTRAN model. For different element sizes, the microplane model requires re-calibration of the input parameters, and then a different coupling time step may be more appropriate.

While beyond the scope of this study, a more thorough verification effort could better reveal our model's limitations with respect to scenarios that we do not simulate here, such as for significantly faster or slower injection rates or for domains and meshes of different sizes. Researchers have developed suite of analytical and numerical solutions for propagating hydraulic fractures that address issues such as viscosity-dominated and toughness-dominated regimes more precisely than the classic KGD solutions, as shown in (Detournay, 2004; Garagash and Detournay, 2005; Adachi and Detournay, 2008; Lecampion et al., 2013). Such tools will be key to future studies to explore the limits of our coupled HOSS-PFLOTRAN model and explore more of the mechanisms that could give rise to crack branching. Here, the classic KGD analytical solutions enable us to validate the timestep that we use for HOSS-PFLOTRAN coupling. This is a first-order model verification.

6. Mechanisms of hydraulic fracture branching

We use three-dimensional HOSS-PFLOTRAN modeling to investigate the conditions that cause hydraulic fracture branching. As shown in Fig. 5a, the model has a dimension of $1.1\,m \times 2.1\,m \times 1.1$ m and is subjected to *in-situ* stresses of 44.8 MPa (x), 47.6 MPa (y), and 60.7 MPa (z). Table 2 lists the major input hydromechanical properties in the simulation, except for the microplane model's parameters that are calibrated for shales and reported in Li et al. (2017). The microplane model handles fracture creation in any element of the hexahedral meshes, whether or not a fracture or weak layer is seeded at the start of modeling.

We choose the values of the parameters in Table 2 to relate our simulations to the Marcellus shale formation. The boundary nodal displacement is fixed at zero in the normal direction at $y = 0$. The other boundaries are set at constant stress. We further assign Neumann boundary conditions of zero fluid flux to all the six boundaries, except at the hydraulic fracture initiation zone where a constant flux of 0.12 m/s is specified. This constant injection flux is equivalent to a plane-strain injection rate of 0.012 m^2/s, which is likely greater than a typical plane-strain injection rate in the field (Mayerhofer et al., 2011). We choose the large injection rate for numerical efficiency reasons. The large injection rate can also provide insight on proper selection of injection rates in field practice to encourage complex hydraulic fracture structures. To investigate hydraulic fracture branching mechanisms, we complete the three simulation scenarios shown in Fig. 5 (b, c, and d).

In the first scenario, we define one hydraulic crack with an initial aperture of 0.1 mm perpendicular to the minimum horizontal stress (Fig. 5b). All the other elements are assigned the matrix properties in Table 2. The Biot stress coefficient in x direction, α_x, which affects the effective stress in x direction, is allowed to increase as the local cracking damage accumulates. Fig. 6 shows the simulation results. The hydraulic fracture (red vertical plane) only propagates along the maximum horizontal stress (Fig. 6a to 6d). Fig. 6e shows the evolution of effective normal stresses along line L-L' that is defined in Fig. 6d. For both early and late times, the effective normal stresses in x direction, σ'_{xx}, and in y direction, σ'_{yy}, remain negative (i.e., compressive) at both sides of the hydraulic fracture. Therefore, hydraulic fracture branching is impossible in this case. The Biot stress coefficient in x direction, α_x, increases to 1.0 only in the hydraulic fracture. The Biot coefficient in the y direction remains at the initially specified value. This result is consistent with the experimental observations in which the fractured rock exhibits increased Biot stress coefficient in the direction normal to the crack plane (Shao, 1998; Xie et al., 2012).

Table 2
Input parameters of HOSS-PFLOTRAN coupling model for fracture branching simulations.

Parameter	HOSS-PFLOTRAN model	Note
Young's modulus E (GPa)	25.0	Spherocylindrical microplane model inputs calibrated for shales (Li et al., 2017).
Poisson's ratio ν	0.19	
Initial Biot stress coefficient α_0	0.5	
Matrix uniaxial compressive strength (MPa)*	30.10	
Matrix tensile strength (MPa)*	1.73	
Weak layer uniaxial compressive strength (MPa)*	27.10	Assumed to be 10% weaker than the matrix
Weak layer tensile strength (MPa)*	1.56	
Porosity (%)	10.0	Marcellus shale (Khalil and Emadi, 2020)
Matrix permeability (m^2)	4.93×10^{-20}	Marcellus shale (Zamirian et al., 2016)
Weak layer's initial permeability (m^2)	4.93×10^{-17}	Assumed to be three orders greater than matrix
Injection flux q (m/s)	0.12	Assumed
Fluid viscosity μ (mPa·s)	0.89	Marcellus shale reservoir in Pennsylvania (Mayerhofer et al., 2011)
Initial pore pressure (MPa)	27.6	
In-situ vertical stress (MPa)	60.7	
In-situ maximum horizontal stress (MPa)	47.8	
In-situ minimum horizontal stress (MPa)	44.6	

* These mechanical properties are obtained from the uniaxial compression and uniaxial tension simulations that employed the spherocylindrical microplane model in HOSS.

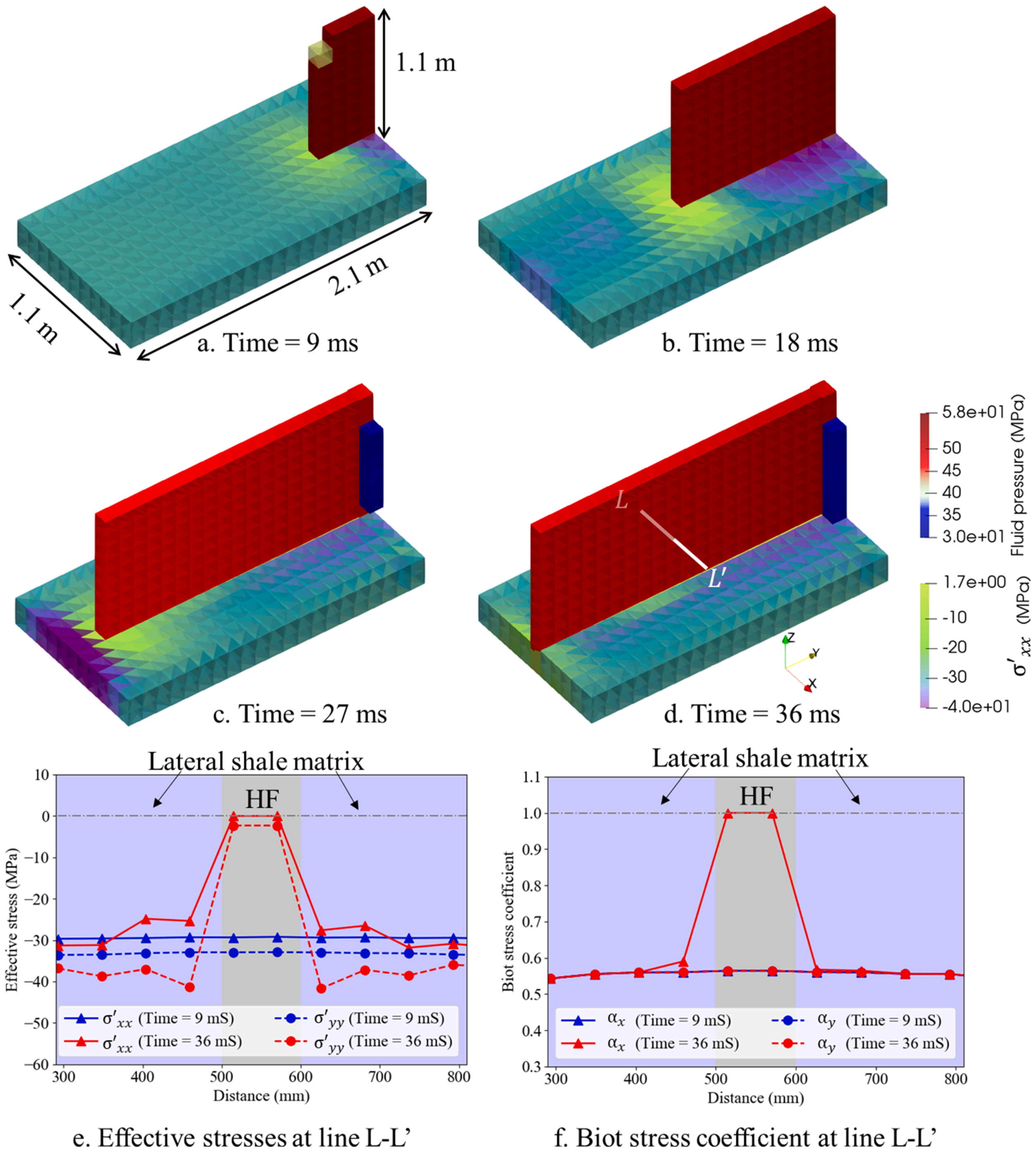

Fig. 6. Results of the first model scenario (Fig. 5b). Hydraulic fracture does not branch without a pre-existing weak layer (a to d). Effective stresses and Biot stress coefficient along the line L-L' (Fig. d) is plotted in (e) and (f). At both sides of the hydraulic fracture, the effective stresses, $\sigma_{xx}^{'}$ and $\sigma_{yy}^{'}$, remain negative (i.e., compressive). Fracture propagation only increases the Biot coefficient, α_x within the fractured elements.

In the second scenario (Fig. 5c), we incorporate a pre-existing weak layer that is perpendicular to the preferred propagation direction of hydraulic fracture. This pre-existing weak layer has a tensile strength that is 90% of the matrix strength (Table 2). The weak layer is initially closed but has a permeability that is 1000 fold greater than the matrix permeability. Other parameters remain the same as in the first scenario. Introducing this closed weak layer does not change the fracture pattern after injection. The hydraulic fracture continues propagating along the maximum horizontal stress direction after crossing the weak layer despite some pressure diffusion into the weak layer (Fig. 7a to 7d). The effective normal stresses, $\sigma_{xx}^{'}$ and $\sigma_{yy}^{'}$, still remain negative at both sides of the hydraulic fracture

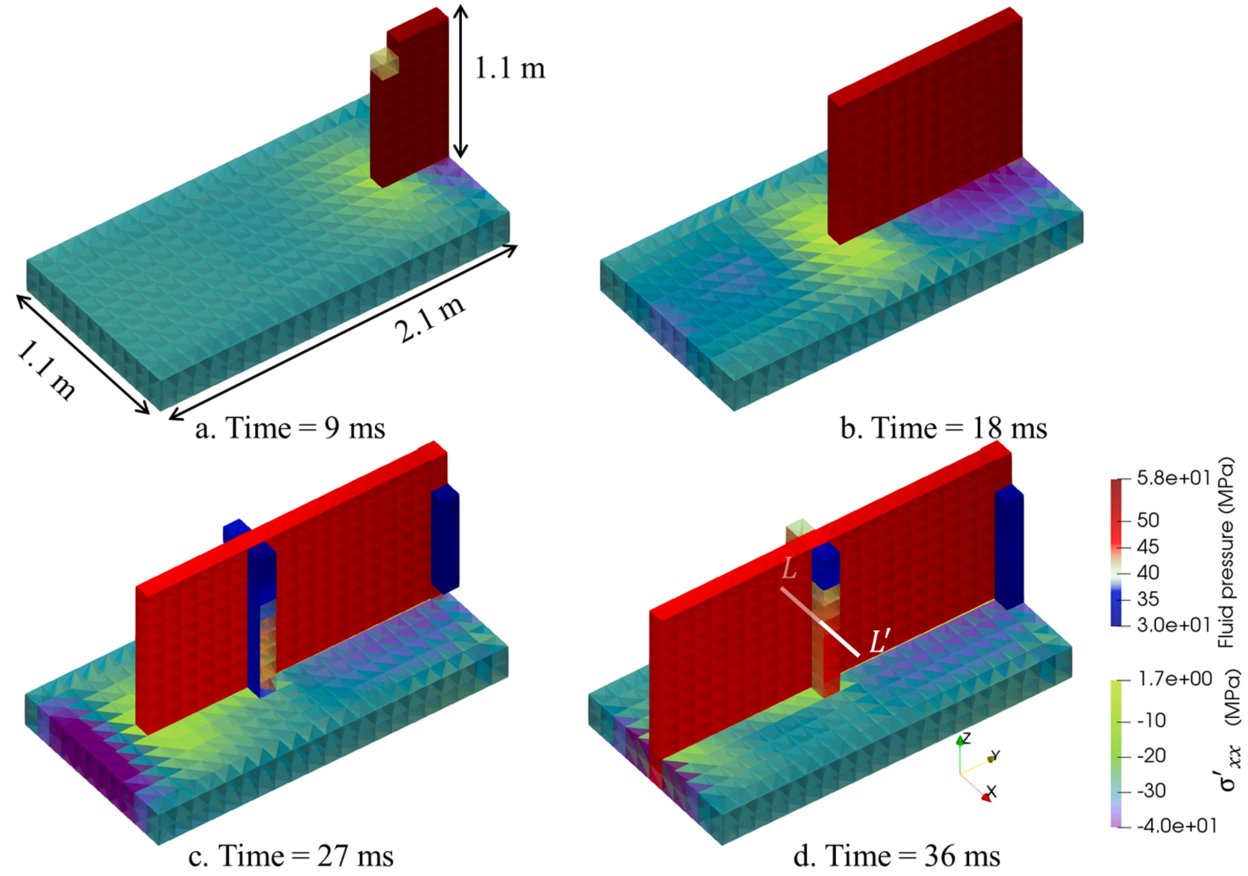

a. Time = 9 ms

b. Time = 18 ms

c. Time = 27 ms

d. Time = 36 ms

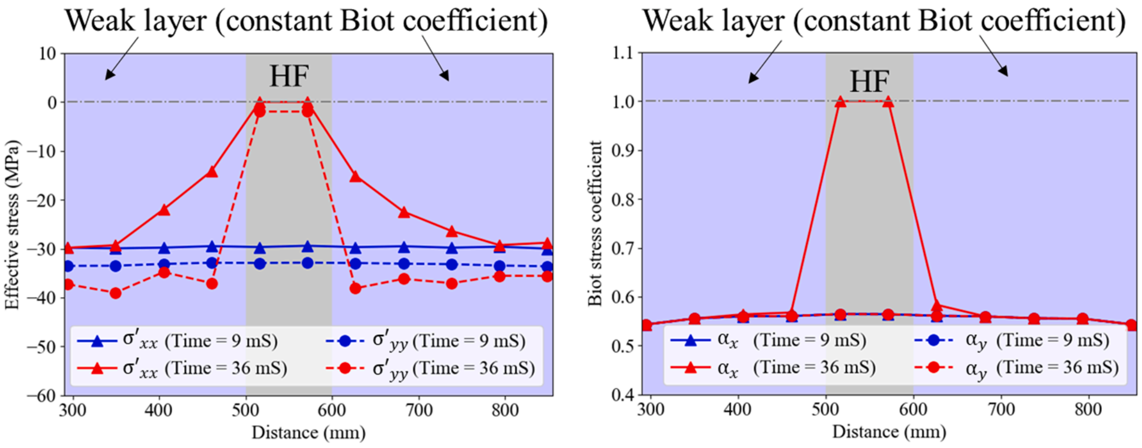

e. Stress changes at line L-L’

f. Biot stress coefficient at line L-L’

Fig. 7. Results of the second model scenario (Fig. 5c). Hydraulic fracture does not branch when Biot coefficient in y direction α_y is independent from inelastic strain accumulation at the pre-existing weak layer (a to d). The weak layer has a greater initial permeability than the matrix, therefore, fluid pressure increases in the weak layer after the hydraulic crack crosses it (c and d). This increased fluid pressure reduces the effective stresses, $\sigma_{xx}^{'}$ and $\sigma_{yy}^{'}$, along the line L-L’ at in the lateral weak layer (e), but the effective stresses remain negative (i.e., compressive), so fracture branching did not occur in this case. The Biot stress coefficient α_y does not increase with accumulating damage in the pre-existing weak layer (f).

(Fig. 7e). In Fig. 7f, the anisotropic Biot stress coefficients change similar to the previous case. Therefore, the existence of a permeable closed weak-layer is not enough to cause hydraulic fracture branching.

In the third scenario (Fig. 5d), we use the same setup as in the second model but take into account the damage dependence of the

Biot stress coefficient in the *y* direction in the pre-existing weak layer. After the hydraulic fracture crosses the weak layer, fluid starts to pressurize the micro-cracks and the damage starts to accumulate. During this process, the Biot stress coefficient increases in the direction perpendicular to the crack growth direction. Unlike the second scenario where the increasing Biot stress coefficient in the *y* direction was excluded, in this third scenario we find that fracture branching occurs after the primary hydraulic crack crosses the weak layer (Fig. 8a to 8d). Fracture branching causes simultaneous growth of vertical cracks in orthogonal directions under the anisotropic far-field horizontal stress condition. Fig. 8f shows the increased Biot coefficient in the *y* direction (α_y) of the weak layer after hydraulic

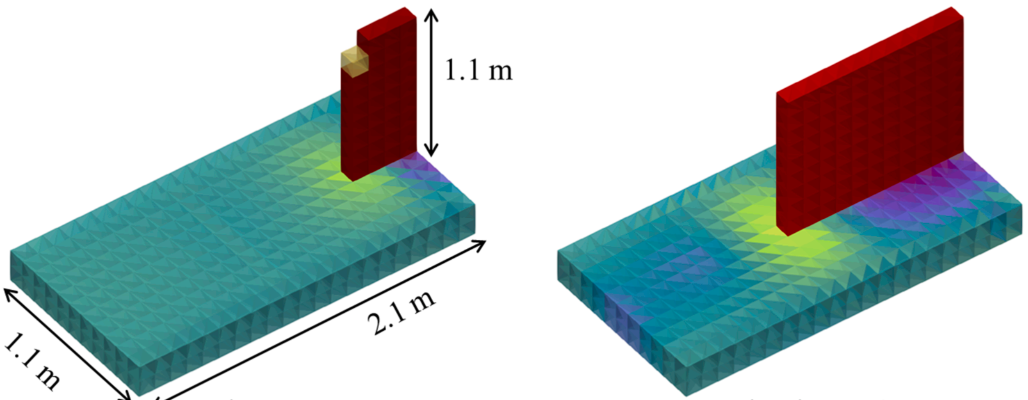

a. Time = 9 ms

b. Time = 18 ms

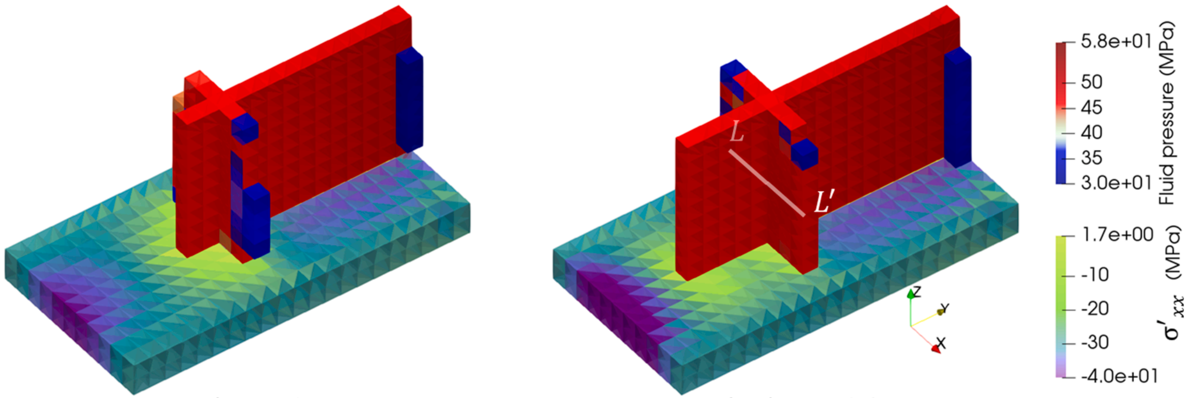

c. Time = 27 ms

d. Time = 36 ms

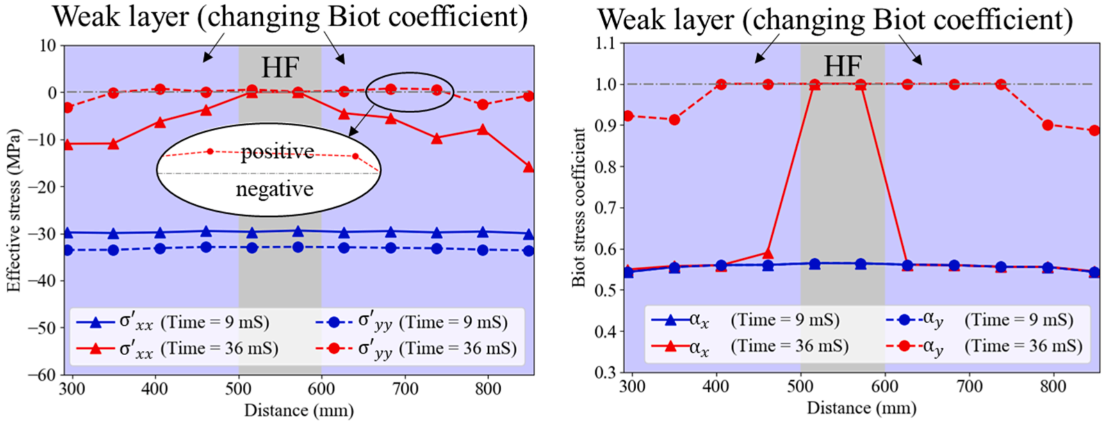

e. Stress changes at line L-L’

f. Biot stress coefficient at line L-L’

Fig. 8. Results of the third model scenario (Fig. 5d). Hydraulic fracture branches when the tensorial Biot coefficients of a pre-existing weak layer increase during damage accumulation (a to d). The fluid pressure increases quickly in the weak layer after the hydraulic crack crosses it (c and d), resulting in simultaneous growth of sideways branched hydraulic cracks. Unlike the previous two cases, the Biot coefficient of the weak layer in the *y* direction, α_y, increases to 1.0 (f), causing the effective stress, to become positive (tension) in the weak layer (e).

fracture branching. This increasing Biot coefficient α_y eventually generates positive (tensile) effective stress σ'_{yy} in the weak layer (Fig. 8e).

Our simulation results demonstrate that sideways hydraulic fracture branching from the crack face can occur for the given weakly anisotropic horizontal stresses shown in Fig. 5 when (1) permeable weak layers exist and (2) the anisotropic Biot stress coefficient changes as the damage accumulates. The selected boundary stresses match the stress condition of a Marcellus shale reservoir in

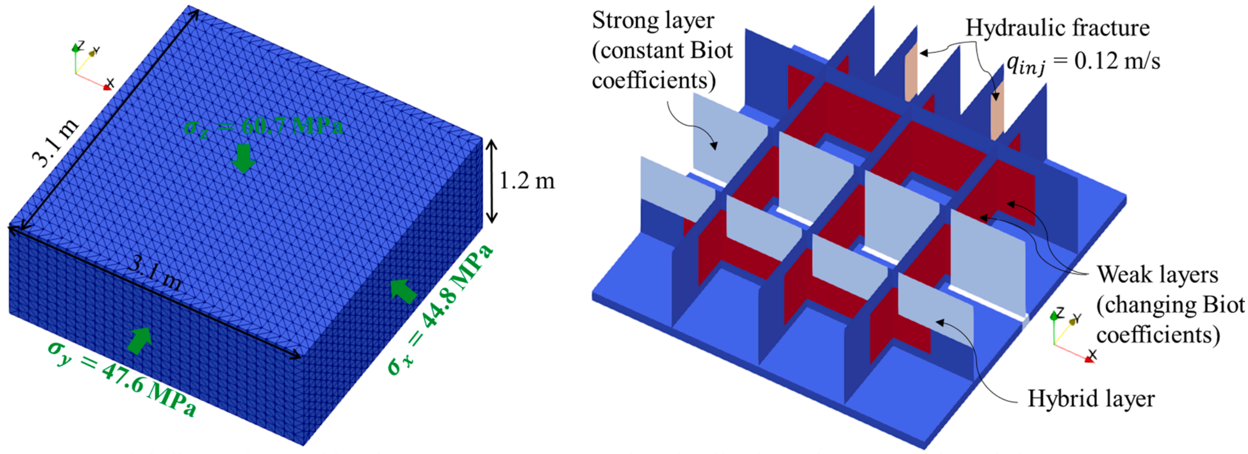

a. Model dimension and in-situ stresses

b. Distribution of strong and weak layers

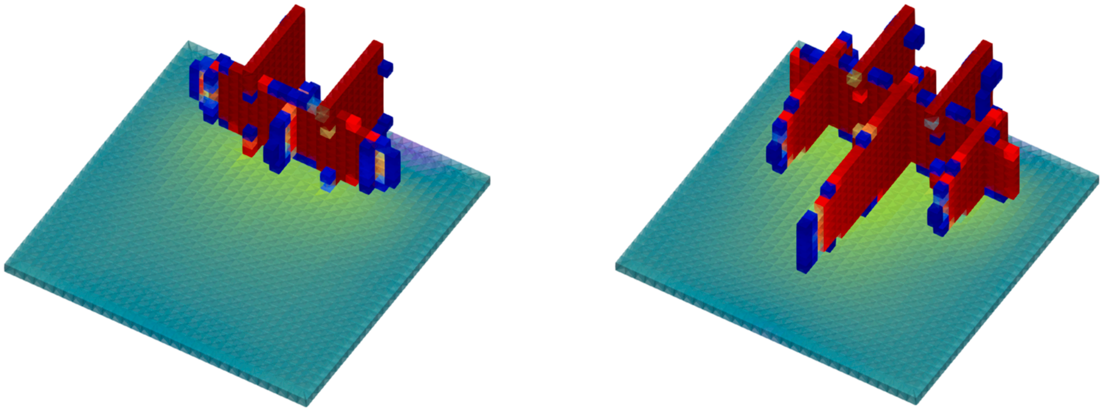

c. Time = 22.8 ms

d. Time = 39.6 ms

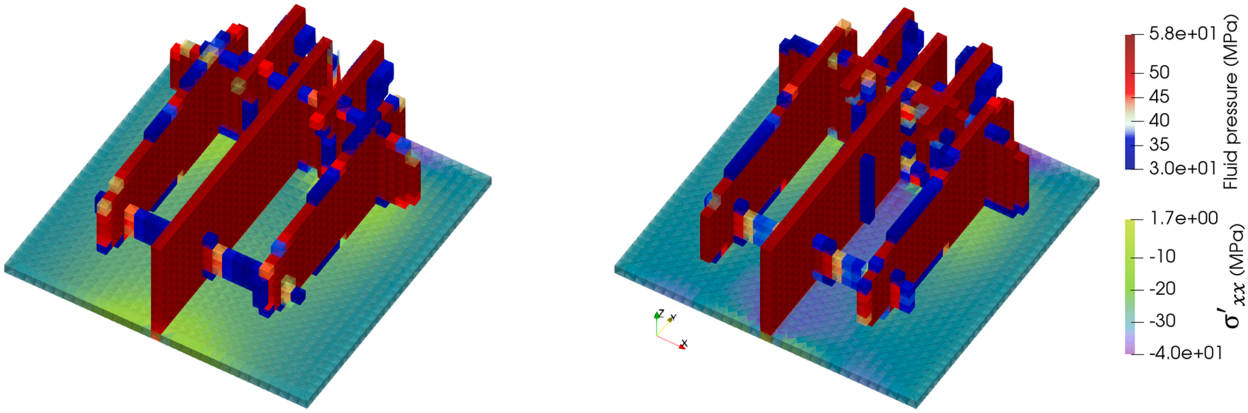

e. Time = 73.2 ms

f. Time = 90.0 ms

Fig. 9. A three-dimensional model (a) having a mixture of intact (matrix), weak, and strong layers (b). Progression of hydraulic fracturing and branching in the three-dimensional model containing weak and strong layers (c to f). Fluid injection opens all the weak layers but not the strong layer. Fluid pressure builds up at the intersections between the hydraulic cracks and the strong layers, due to a higher permeability relative to the matrix.

Pennsylvania (Mayerhofer et al., 2011). Stronger horizontal stress anisotropy is known to inhibit hydraulic fracture complexity (Kresse et al., 2013). Our proposed poromechanical mechanism for fracture branching will now enable quantitative prediction of the limits of stress anisotropy toward inhibiting fracture complexity. Further, injection of low-viscosity fluid can promote growth of complex fracture networks while injection of high-viscosity fluid promotes planar hydraulic fracture paths, as summarized in Bunger and Lecampion (2017). Future studies are needed to quantify the dependency of fracture branching on stress anisotropy and injection parameters so that field practices can be optimized. Our HOSS-PFLOTRAN coupling provides a 3D numerical modeling tool to pursue these future studies. In the next section, we present some case studies to demonstrate how the proposed poromechanical mechanism impacts fracture complexity in 3D networks.

7. Examples of complex patterns of 3D hydraulic fractures

Complex patterns of 3D hydraulic fractures have been extensively observed in the field (Le Calvez et al., 2007; Gale et al., 2018), which is often attributed to the interaction of hydraulic fractures and complex natural fractures at the tip region of hydraulic fractures (Renshaw andPollard, 1995). Here, we present 3D simulations that demonstrate hydraulic fracture branching behind the fracture tip to better explain field observations of complex crack structures.

7.1. Combination of pre-existing strong and weak layers

Now we introduce one example where a 3D hydraulic fracturing model is required to simulate the complex crack patterns in the deep reservoir conditions. The numerical model has a dimension of $3.1\ m \times 3.1\ m \times 1.2$ m with the anisotropic *in-situ* stresses illustrated in Fig. 9a. Two vertical hydraulic fractures are defined at the edge $y = 3.1$ m, where a constant injection flux of 0.12 m/s is defined. Six pre-existing vertical discontinuities are incorporated into the model (Fig. 9b). Weak layers with high initial permeability and low tensile strength (Table 2), comparing to the surrounding rock matrix, are included as shown. Also, strong layers are included that have the same tensile strength as the matrix along with the high permeability that is 1000 fold higher than that of the matrix. The strong and weak layers are mixed to provide an example with three-dimensional complexity. The matrix porosity, permeability, and hydromechanical properties are summarized in Table 2.

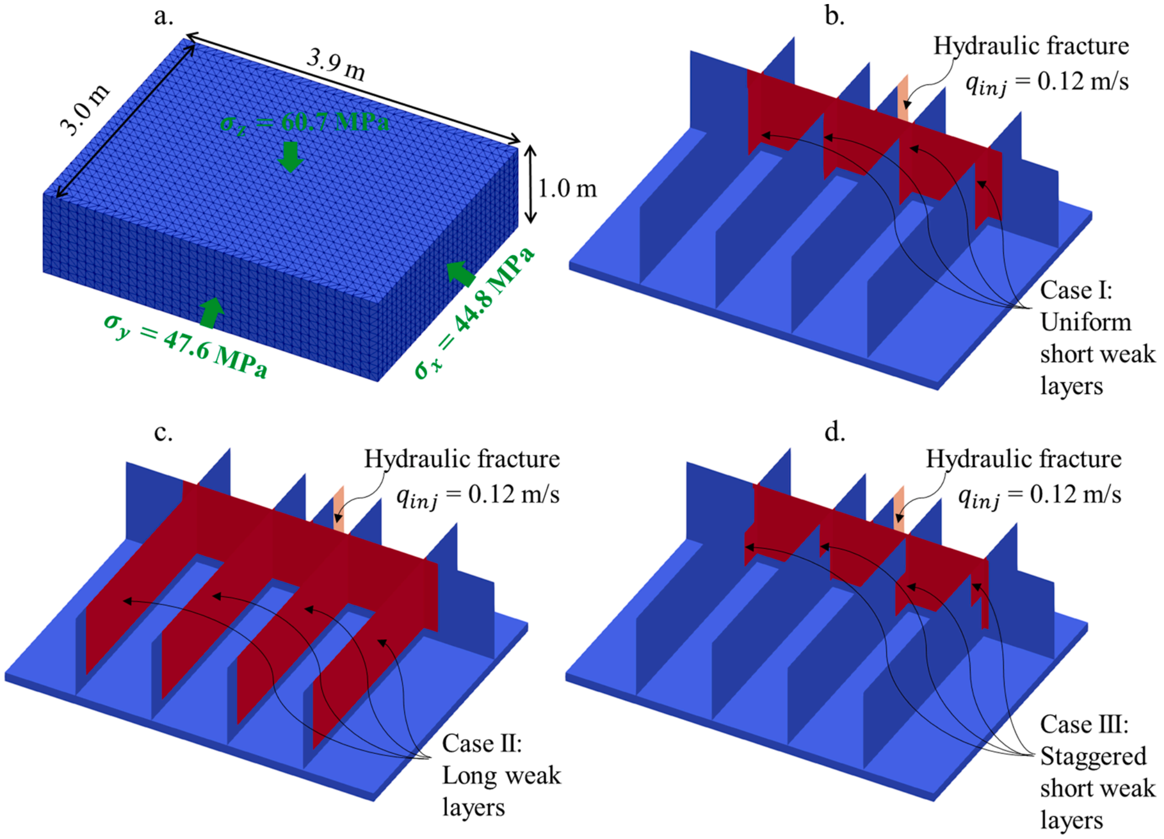

Fig. 10. Model geometry, *in-situ* stresses, and the three cases used to investigate simultaneous growth of closely spaced hydraulic fractures with the stress shadowing effect. Four short weak layers are uniformly spaced in the first case (b), whereas all four weak layers are extended in the second case (c). In the third case, all the four weak layers are reduced to half height and staggered (d).

The setup of the pre-exiting discontinuities in Fig. 9b is motivated by field observations that the natural fractures in unconventional hydrocarbon reservoirs have varying degrees of mineral cementation (Gale et al., 2007). For example, in the Barnett shale, natural fractures are predominately sealed with calcite and have weaker tensile strengths than rock matrix (Gale et al., 2007). In Woodford shale, however, natural fractures are more frequently found to be sealed with quartz and have strength and stiffness comparable to rock matrix (Gale et al., 2007; Lander and Laubach, 2015).

The simulation results are shown in Figs. 9c to 9f. The horizontal plane shows the effective stress distribution while the vertical planes illustrate the distribution of fluid pressure in the hydraulic cracks. Hydraulic fractures open all the four pre-existing weak layers and the bottom-half (weak) of the hybrid layer. Excess fluid pressure builds up at the intersection between the strong layer and the weak layers due to the high initial permeability of the strong layer (Fig. 9f: blue elements at center of model). However, this excess fluid pressure is not large enough to open and propagate the strong layer.

7.2. *Stress shadowing versus fracture swarming and parallel crack instability*

In this section, we perform simulations to investigate simultaneous growth of closely spaced hydraulic fractures with the stress shadowing effect, which is a consequence of bifurcation instability in the propagation of parallel hydraulic cracks (Bažant et al., 2014). Stress shadowing refers to the stress interactions in an array of parallel hydraulic fractures in which the growth of one hydraulic fracture perturbs the stress on the neighboring parallel cracks. In other words, this is the loss of stability of parallel crack propagation in which the extension of one crack suppresses the growth of the neighboring cracks. Importance of this topic for hydraulic fracturing treatments in unconventional hydrocarbon reservoirs was also numerically demonstrated by Bunger et al. (2012). Previous study inducates that under certain conditions, e.g., when the fluid pressure profiles along the crack do not have a steep pressure drop, the instability (loosely termed stress shadowing) never develops, and densely spaced parallel cracks must grow (Bažant et al., 2014). Indeed, in a recent field study, researchers observed an array of densely spaced hydraulic fractures (popularly termed as “fracture swarming”) in rock core that was collected after a fracturing treatment (Gale et al., 2018). This observation raises the question of what are the precise conditions that decide whether stress shadowing or fracture swarming, i.e., instability or not, would dominate crack growth in deep reservoirs.

Using the model geometry and *in-situ* stresses shown in Fig. 10a, we investigate three cases of pre-existing weak layers. In the first case (Fig. 10b), four short weak layers are uniformly spaced (0.7 m). These four weak layers are substantially longer in the second case (Fig. 10c). In the third case (Fig. 10d), all the four short weak layers are reduced by half in height and distributed in a staggered manner. Again, Table 2 lists the material parameters in the simulations. In each simulation case, a constant injection flux of 0.12 m/s is

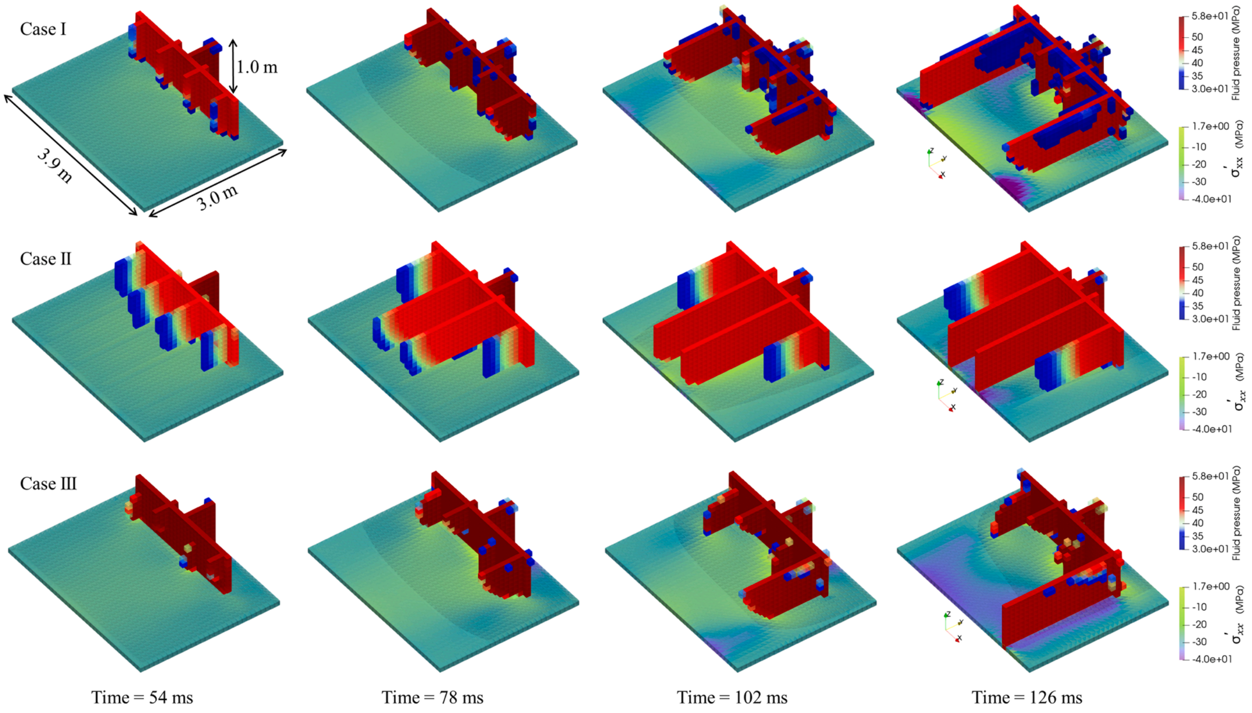

Fig. 11. Simulation results of the three cases. In the first case (top row) where four short weak layers are uniformly spaced, the simulation indicates fast-growing outer cracks, which creates a strong stress shadowing effect that significantly delays the propagation of the inner cracks. In the second case (middle row) where four weak layers are extended in length, all four fractures continue to propagate for the full duration of the simulation. In the third case (bottom row) where the four weak layers are reduced in height and are spatially staggered, fast growth of one fracture creates a strong stress shadowing effect that retards the propagation of the other cracks.

specified at the injection zone (light orange in Fig. 10), which is equivalent to a constant volumetric injection rate of 0.012 m^3/s because the injection area remains as 0.1 m^2. Fluid partitioning into the branched hydraulic fractures is calculated by PFLOTRAN.

Results for the first simulation case are shown in the first row in Fig. 11. The horizontal plane illustrates the effective stress while the vertical planes depict the fluid pressure in the hydraulic cracks. At early times ($\leq$ 54 ms), all four short weak layers are opened and start to grow. However, the two outer cracks grow much faster at later times ($\geq$ 78 ms), which is a consequence of the instability of parallel cracks, or stress shadowing that significantly delays the growth of the inner two cracks, similar to that seen in the work of Gunaydin et al. (2021). It is notable that the fluid flow path is longer for these outer fractures, which will incur greater pressure losses, but the shadowing effect still dominates. By the end of the simulation, the lengths of the inner cracks are 0.4 − 0.5 m, only 17% − 21% of the outer fracture lengths. It appears that fracture branching also promotes multi-stranded fracture propagation.

In the second case, where the pre-existing weak layers are extended in length, all four hydraulic fractures grow simultaneously (second row in Fig. 11). One interesting phenomenon is that the inner cracks propagate faster than the outer cracks. Although the outer cracks grow at a slower rate, their lengths account for 70% − 78% of the lengths of inner cracks by the end of the simulation. This is distinctly different from the first case. Despite the weak layers having tensile strengths that are 90% of the matrix, it is unlikely that this difference in tensile strength, 0.17 MPa (Table 2), is profound enough to cause the simultaneous propagation of all hydraulic fractures. Instead, changes in the Biot stress coefficient in the transverse direction in the pre-existing weak layers allows the effective stress to increase from negative (compressive) to positive (tensile). This is the mechanism that competes with the stress shadowing of the fast-growing nearby cracks, promoting the simultaneous propagation of all four fractures in the second case. Fu et al. (2020) speculated, using numerical models, that scaling-down the fracture toughness of clustered pre-existing cracks might explain "fracture swarming". However, our model demonstrates a different cause: time-dependent progressive damage accumulation.

In the third case, the weak layers are reduced in size and are spatially distributed in a staggered manner. Our initial expectation was simultaneous growth of all four cracks because the stress shadowing effect would be diminished due to the staggered spatial distribution of the weak layers. However, the 3D model predicted an interesting result where the propagation of one outer fracture dominated the system (the third row in Fig. 11). At early times ($\leq$ 54 ms), all the four short weak layers are opened. As injection continues ($\geq$ 78 ms), one outer fracture quickly attains the full height of the model and then grows faster in the direction parallel to the maximum horizontal stress. This fracture creates strong compressive stress in the normal direction and significantly retards, yet does not halt, the growth of the other cracks. By the end of simulation, the three short fractures reach only to 22% − 35% of the dominant fracture length.

These three simple cases with pre-existing weak layers show how the resultant fracture patterns are strikingly different, depending on the heterogeneous properties of the rock. In the real subsurface, pre-existing weak layers can possess much more complex structures and geometries, so our cases only represent a small fraction of what could be possible. Our simulation clearly demonstrates that the 3D hydraulic fracturing simulator is necessary to attain good understanding of the complex hydraulic fracturing mechanisms. Intuitively, one would expect that stress shadowing would retard or even suppress the growth of nearby cracks once a dominant hydraulic fracture starts to propagate. However, uniformity of pressure distribution along the cracks and progressive anisotropic Biot coefficient increase can overwhelm stress shadowing to promote multiple-fracture propagation.

We should note that, stress shadowing only happens when one crack is slightly longer than another. In the case of equally long cracks with equal properties and stress conditions, bifurcation and stability analysis is needed to predict which fracture will dominate over the others. Theoretical studies have been conducted to assess crack bifurcation and stability based on the matrix of derivatives of the stress intensity factors (Bažant and Wahab, 1979; Bažant et al., 2014). Those studies showed that the bifurcation of the evolution path of parallel cracks can result in differences in crack growth rates if the hydraulic pressure profile along the parallels crack decreases fast enough. When the hydraulic pressure profile along the cracks is nearly uniform and material properties are homogeneous, no bifurcation and no stress-shadowing is predicted. A more complete bifurcation and stability analysis of cracks is a subject for future study.

Finally, we must point out that there are rate dependent effects that influence branching of hydraulic fractures. As demonstrated in our previous experimental study (Li et al., 2021a), fluid injection rate, fluid viscosity, and permeability of the weak layers all influence the fracture branching process. This experimental work also discovered that intermediate injection rates and viscosities can best promote branching. Here, we used fracture branching as a test case for 3D HOSS-PFLOTRAN coupling, even though this modeling method is not optimal to investigate field scale fracture branching processes due to limitations from the small time steps. However, our study shows that hydraulic fracture branching and swarming can occur rapidly - in milliseconds - when fluid penetrates into weak layers. In addition, our simulations reveal that complex fracture branching and swarming can occur at the meter-scale, so it is reasonable to expect that it will also occur at larger scales. These results justify future efforts to implement a damage dependent Biot coefficient in larger scale modeling tools.

8. Conclusion

In this study, we present a sequentially coupled numerical modeling tool, HOSS-PFLOTRAN, to investigate three-dimensional hydraulic fracture branching in the subsurface. Fracture creation and propagation are computed based on the spherocylindrical microplane constitutive model implemented with the crack-band theory. We verify the HOSS-PFLOTRAN model using the classic 2D plain-strain KGD solution without fluid leak-off at fracture walls. Through three simulations, we demonstrate that hydraulic fractures can branch into pre-existing permeable weak layers when damage dependent Biot effective stress coefficients are considered. This finding provides a poromechanics-based explanation for hydraulic fracture branching in heterogeneous reservoirs. This adds to the current understanding of the causes for crack branching that include complex near-wellbore stress states, layered/localized stress heterogeneity, and extreme reservoir and injection parameters.

Pre-existing geological discontinuities are not always weaker and more permeable than the surrounding rock matrix. Particularly, mineral deposition in the cracks, million years of crack closing due to secondary creep (or nonlinear viscous flow), microcrack healing and geological diagenesis certainly reduce permeability, although microscale permeability in the damaged weak layer along the sealed crack or along the interface between the mineral deposit and shale surely remains an important factor. We present a numerical model where pre-existing weak and strong layers concurrently exist close to a hydraulic fracture. We consider that weak layers contain disconnected micro cracks that increase the Biot stress coefficient and make it anisotropic, as the damage accumulates during fluid infiltration. Our simulation predicts that hydraulic fractures branch into the weak layers, but not into the strong layers. This result demonstrates that three-dimensional numerical models are needed to account for heterogeneous hydromechanical properties and pre-existing geological discontinuities. Such models can help unveil the mechanisms for complex hydraulic fracture networks in the subsurface.

Our case studies demonstrated that fracture branching with simultaneous growth of multiple fractures (including offset parallel fractures) can be predicted if we consider (1) the damage-dependent Biot effective stress coefficients and (2) geologic discontinuities in low-anisotropy stress scenarios. Furthermore, our results demonstrate the potential of our 3D coupled HOSS-PFLOTRAN model to systematically explore the scenarios that promote or inhibit crack branching. Specifically, our simulations showed simultaneous growth of closely spaced hydraulic fractures amidst the stress shadowing effect. This result is counterintuitive to conventional thinking where stress shadowing is expected to inhibit the simultaneous growth of closely spaced parallel fractures. Our results also showed that 3D effects, the continuity of weak layers, and probably also pressure distribution along the cracks could be key factors for promoting crack branching. With respect to field observations, our simulations could help to explain the formation of long dense parallel cracks (also called hydraulic fracture “swarming”). Overall, this study presents our new modeling tool and preliminary results that demonstrate crack branching by a poromechanical mechanism. A detailed investigation to identify implications for predictive trends in field scale processes is a subject for future work.

Ultimately, we introduced and validated a three-dimensional hydraulic fracturing simulator, HOSS-PFLOTRAN, that is capable of predicting complex hydraulic fracturing behavior. This model currently considers only orthogonal pre-existing weak layers to remove the complication of shear fractures. While the results do reveal possible mechanisms for fracture branching and extended parallel crack propagation (“swarming”), more study is needed to explore deeper the critical conditions that govern complex fracture behaviors. For example, injection of high-viscosity fracturing fluid could delay fluid penetration into pre-existing weak layers, potentially delaying or preventing fracture branching (Chen et al., 2020; Li et al., 2021a and 2021b).

Our ultimate goal is to propose a scaling relationship that can predict the injection parameters that promote (or inhibit) fracture branching with the consideration of stress anisotropy and reservoir heterogeneity (i.e., the contrast of poromechanical properties between rock matrix and pre-existing geological discontinuities). In a recent experimental and theoretical study (Li et al., 2021a), we established a preliminary relationship between injection parameters and reservoir heterogeneity for promoting or inhibiting hydraulic fracture branching. Building this HOSS-PFLOTRAN 3D simulator now allows us to further investigate hydraulic fracture branching by considering: (1) the degree of reservoir heterogeneity that spans higher orders of magnitude; (2) realistic magnitudes and anisotropy of *in-situ* stresses, and (3) three-dimensional effects that include stress shadowing. This study focuses on presenting this modeling tool and showing its potential to help make progress towards our ultimate goal.

Declaration of Competing Interest

The authors declare that there is no known competing financial interests or personal relationships that could have appeared to influence the work reported in this paper.

Data availability

Data will be made available on request.

Acknowledgments

The authors are grateful to the funding support from the U. S. Department of Energy (DOE) Basic Energy Sciences (LANLE3W1). Partial supplementary funding was obtained under NSF Grant CMMI-202964 to Northwestern University. This research used resources provided by the Los Alamos National Laboratory Institutional Computing Program, which is supported by the U.S. Department of Energy National Nuclear Security Administration under Contract No. 89233218CNA000001. There is no conflict of interest per the author’s knowledge. The authors declare no data used in this work.

Appendix

In PFLOTRAN, we solve single phase, fully saturated, isothermal fluid flow using the following governing mass conservation equation.

$$\frac{\partial}{\partial t}(\phi\eta) + \nabla \cdot (\eta \boldsymbol{q}) = Q_w \tag{A1}$$

In the above equation, Darcy flux $\boldsymbol{q}$ is defined in the following expression.

$$\boldsymbol{q} = -\frac{\boldsymbol{k}}{\mu}\nabla(p - \rho g z) \tag{A2}$$

In Eqs. (A1) and (A2), ϕ is porosity. η is molar water density in kmol/m^3. $\boldsymbol{q}$ is Darcy flux in m/s. $\boldsymbol{k}$ is permeability In m^2. μ is fluid dynamic viscosity in Pa·s. p is fluid pressure in Pa. g is the gravitational acceleration in m/s^2. ρ is density of the compressible injection fluid. Q_w denotes the source/sink term and has the following expression.

$$Q_w = \frac{q_M}{W_w}\delta(\boldsymbol{r} - \boldsymbol{r}_{ss}) \tag{A3}$$

q_M denotes fluid mass rate in kg/(m^3·s). W_w is the molecular mass of injection fluid in (kg/kmol). $\boldsymbol{r}_{ss}$ is the location of the source/sink.

In our hydraulic fracturing simulations, HOSS solves for the nodal displacements and forces in the solid domain, which allows us to compute fracture apertures according to the spherocylindrical microplane constitutive model (Eqs 1–1 and 1–2). The fracture apertures are sent to PFLOTRAN to update the porosity (i.e., storage) of the cracked elements when solving the governing fluid mass conservation equation.

Next, we introduce the concept of the spherocylindrical microplane constitutive model. This model was developed by Li et al. (2017) to specifically address the challenges of modeling mechanical failure and inelastic fracturing localization of shales. The main idea is to couple a cylindrical microplane system in parallel to the classical spherical microplane system for handling progressive softening damage in shales. Each system is subjected to the same strain tensor while their stresses are added according to the partition of unity concept. In both the spherical and cylindrical systems, the strain vectors on any microplane are the resolved components of the macro-continuum strain tensor. Therefore, the microplanes are subjected to a kinematic constraint, which ensures the stability of strain softening and guarantees a robust explicit numerical algorithm.

The spherocylindrical microplane model accounts for both elastic and inelastic behavior on the microplanes. Consideration of the elastic behavior on the microplanes is straightforward. The inelastic behavior occurs when crossing the so-called stress-strain boundaries that can be regarded as strain-dependent strength limits. These stress-strain boundaries include a tensile stress boundary for the spherical phase, a tensile and compressive deviatoric stress boundary for the spherical phase, a shear stress boundary for the spherical phase, a compressive volumetric stress boundary for the spherical phase, and a tensile and compressive normal stress boundary for the cylindrical phase. Within these boundaries, the material mechanical response is considered to be elastic. If the boundaries are exceeded in a finite time step or loading step, the stress is decreased, at constant strain, to the boundary and material damage accumulates. The tensile stress-strain boundaries of the microplanes for the spherical and cylindrical phases need to be exceeded in order to initiate and propagate tensile hydraulic fractures. Below we show the coefficients that are defined in the spherocylindrical microplane model for simulating damage and tensile cracking in shales.

To obtain the coefficients in the spherocylindrical microplane model, we tune them to match the modeled and measured stress-strain behavior of a specific material, with a fixed mesh size for the model. These coefficients are dimensionless and include a group of easily scalable parameters (k_i, $i = 1,2,3,4,5$) and another group of hard-to-adjust parameters (c_i, $i = 1, 2, \ldots, 18$). In the present study, the optimized parameters are $k_1 = 70.0\text{E-}6$, $k_2 = 110.0$, $k_3 = 30.0$, $k_4 = 100.0$, and $k_5 = 1.0$. For the hard-to-adjust parameters, $c_1,\ c_2, \ldots,\ c_{18}$ are 0.2, 2.5, 2.5, 70.0, 8.0, 20.0, 1.3, 12.0, 1.2, 3.0, 3.2, 5.0, 3.1, 9.5, 0.35, 0.02, 0.01, 0.4, respectively. The meaning of these parameters is described in Li et al. (2017). Finally, the codes of the explicit spherocylindrical microplane constitutive model are publicly accessible (Bazant, 2022).

References

Adachi, J.I., Detournay, E., 2008. Plane strain propagation of a hydraulic fracture in a permeable rock. Eng. Fract. Mech. 75 (16), 4666–4694. https://doi.org/10.1016/j.engfracmech.2008.04.006.

Bažant, Z.P. (2022). Coding of the explicit spherocylindrical microplane constitutive model http://www.civil.northwestern.edu/people/bazant/m7-coding/m7_cyc_schell_v1.f. Accessed July 2022.

Bažant, Z.P., Oh, B.H., 1983. Crack band theory for fracture of concrete. Matériaux et construction 16 (3), 155–177. https://doi.org/10.1007/BF02486267.

Bažant, Z.P., Oh, B.H., 1985. Microplane model for progressive fracture of concrete and rock. J. Eng. Mech. 111 (4), 559–582. https://doi.org/10.1061/(ASCE)0733-9399(1985)111:4(559).

Bažant, Z.P., Ohtsubo, H., 1977. Stability conditions for propagation of a system of cracks in a brittle solid. Mech. Res. Commun. 4 (5), 353–366. https://doi.org/10.1016/0093-6413(77)90015-5.

Bažant, Z.P., Ohtsubo, H., Aoh, K., 1979. Stability and post-critical growth of a system of cooling or shrinkage cracks. Int. J. Fract. 15 (5), 443–456. https://doi.org/10.1007/BF00023331.

Bažant, Z.P., Planas, J., 1997. Fracture and Size Effect in Concrete and Other Quasibrittle Materials. CRC press.

Bažant, Z.P., Prat, P.C., 1988a. Microplane model for brittle-plastic material: I. Theory. J. Eng. Mech. 114 (10), 1672–1688. https://doi.org/10.1061/(ASCE)0733-9399(1988)114:10(1672).

Bažant, Z.P., Prat, P.C., 1988b. Microplane model for brittle-plastic material: II. Verification. J. Eng. Mech. 114 (10), 1689–1702. https://doi.org/10.1061/(ASCE)0733-9399(1988)114:10(1689).

Bažant, Z.P., Salviato, M., Chau, V.T., Viswanathan, H., Zubelewicz, A., 2014. Why fracking works. J. Appl. Mech. 81 (10), 101010 https://doi.org/10.1115/1.4028192.

Bažant, Z.P., Wahab, A.B.A., 1979. Instability and spacing of cooling or shrinkage cracks. J. Eng. Mech. 105 (5), 873–889. https://doi.org/10.1061/JMCEA3.0002529.

Blanton, T.L. (1982). An experimental study of interaction between hydraulically induced and pre-existing fractures. In *SPE unconventional gas recovery symposium, Society of Petroleum Eng*ineers. https://doi.org/10.2118/10847-MS.

Bunger, A.P., Detournay, E., Garagash, D.I., 2005. Toughness-dominated hydraulic fracture with leak-off. Int. J. Fract. 134 (2), 175–190. https://doi.org/10.1007/s10704-005-0154-0.

Bunger, A.P., Lecampion, B., 2017. Four Critical Issues For Successful Hydraulic Fracturing Applications. CRC. Press/Balkema. *Chapter 16 in X.-T.Feng, ed., 'Rock Mechanics and Engineering', Vol. 5 (Surface and Underground Projects)*.

Bunger, A.P., Zhang, X., Jeffrey, R.G., 2012. Parameters affecting the interaction among closely spaced hydraulic fractures. SPE J. 17 (01), 292–306. https://doi.org/10.2118/140426-PA.

Caner, F.C., Bažant, Z.P., 2013. Microplane model M7 for plain concrete. I: formulation. J. Eng. Mech. 139 (12), 1714–1723. https://doi.org/10.1061/(ASCE)EM.1943-7889.0000570.

Carol, I., Bažant, Z.P., 1997. Damage and plasticity in microplane theory. Int. J. Solids Struct. 34 (29), 3807–3835. https://doi.org/10.1016/S0020-7683(96)00238-7.

Chau, V.T., Bažant, Z.P., Su, Y., 2016. Growth model for large branched three-dimensional hydraulic crack system in gas or oil shale. Philos. Trans. R. Soc. A 374, 20150418. https://doi.org/10.1098/rsta.2015.0418, 2078.

Chen, M., Bai, M., Roegiers, J.C., 1999. Permeability tensors of anisotropic fracture networks. Math. Geol. 31 (4), 335–373. https://doi.org/10.1023/A:1007534523363.

Chen, Z., Elsworth, D., Wang, M., 2020. Does Low-Viscosity Fracturing Fluid Always Create Complex Fractures? J. Geophys. Res. Solid Earth 125 (9). https://doi.org/10.1029/2020JB020332 p.e2020JB0s.

Cheng, W., Jin, Y., Chen, M., 2015. Experimental study of step-displacement hydraulic fracturing on naturally fractured shale outcrops. J. Geophys. Eng. 12 (4), 714–723. https://doi.org/10.1088/1742-2132/12/4/714.

Clarkson, C.R., Haghshenas, B., Ghanizadeh, A., Qanbari, F., Williams-Kovacs, J.D., Riazi, N., Debuhr, C., Deglint, H.J., 2016. Nanopores to megafractures: current challenges and methods for shale gas reservoir and hydraulic fracture characterization. J. Nat. Gas Sci. Eng. 31, 612–657. https://doi.org/10.1016/j.jngse.2016.01.041.

Detournay, E., 2004. Propagation regimes of fluid-driven fractures in impermeable rocks. Int. J. Geomech. 4 (1), 35–45. https://doi.org/10.1061/(ASCE)1532-3641(2004)4:1(35).

Ferguson, W., Richards, G., Bere, A., Mutlu, U., Paw, F., 2018. Modelling near-wellbore hydraulic fracture branching, complexity and tortuosity: a case study based on a fully coupled geomechanical modelling approach. Proceedings of the SPE Hydraulic Fracturing Technology Conference and Exhibition, Woodlands, TX. https://doi.org/10.2118/189890-MS.

Fjaer, E., Holt, R.M., Horsrud, P., Raaen, A.M., 2008. Petroleum Related Rock Mechanics. Elsevier.

Flewelling, S.A., Tymchak, M.P., Warpinski, N., 2013. Hydraulic fracture height limits and fault interactions in tight oil and gas formations. Geophys. Res. Lett. 40 (14), 3602–3606. https://doi.org/10.1002/grl.50707.

Frash, L.P., Gutierrez, M., Hampton, J., Hood, J., 2015. Laboratory simulation of binary and triple well EGS in large granite blocks using AE events for drilling guidance. Geothermics 55, 1–15. https://doi.org/10.1016/j.geothermics.2015.01.002.

Fu, W., Ames, B.C., Bunger, A.P., Savitski, A.A., 2016. Impact of partially cemented and non-persistent natural fractures on hydraulic fracture propagation. Rock Mech. Rock Eng. 49 (11), 4519–4526. https://doi.org/10.1007/s00603-016-1103-0.

Fu, W., Morris, J., Fu, P., Huang, J., Sherman, C., Settgast, R., Wu, H. & Ryerson, F. (2020). Developing upscaling approach for swarming hydraulic fractures observed at hydraulic fracturing test site through multiscale simulations. *In SPE Hydraulic Fracturing Technology Conference and Exhibition, Society of Petroleum Eng*ineers. https://doi.org/10.2118/199689-MS.

Gale, J.F., Elliott, S.J. & Laubach, S.E., (2018). Hydraulic fractures in core from stimulated reservoirs: core fracture description of HFTS slant core, Midland Basin, West Texas. In *Unconventional Resources Technology Conference, Houston, Texas, Society of Petroleum Eng*ineers. https://doi.org/10.15530/urtec-2018-2902624.

Gale, J.F., Laubach, S.E., Olson, J.E., Eichhubl, P., Fall, A., 2014. Natural fractures in shale: a review and new observationsNatural Fractures in Shale: a review and new observations. AAPG Bull. 98 (11), 2165–2216. https://doi.org/10.1306/08121413151.

Gale, J.F., Reed, R.M., Holder, J., 2007. Natural fractures in the Barnett Shale and their importance for hydraulic fracture treatments. AAPG Bull. 91 (4), 603–622. https://doi.org/10.1306/11010606061.

Garagash, D.I., Detournay, E., 2005. Plane-strain propagation of a fluid-driven fracture: small toughness solution. ASME J. Appl. Mech. 72 (6), 916–928. https://doi.org/10.1115/1.2047596.

Geertsma, J., De Klerk, F., 1969. A rapid method of predicting width and extent of hydraulically induced fractures. J. Pet. Technol. 21 (12), 1571–1581. https://doi.org/10.2118/2458-PA.

Grassl, P., Fahy, C., Gallipoli, D., Wheeler, S.J., 2015. On a 2D hydro-mechanical lattice approach for modelling hydraulic fracture. J. Mech. Phys. Solids 75, 104–118.

Gunaydin, D., Peirce, A.P., Bunger, A.P., 2021. Laboratory experiments contrasting growth of uniformly and nonuniformly-spaced hydraulic fractures. J. Geophys. Res. Solid Earth. https://doi.org/10.1029/2020JB020107 p.e2020JB020107.

Guo, J., Lu, Q., Chen, H., Wang, Z., Tang, X., Chen, L., 2018. Quantitative phase field modeling of hydraulic fracture branching in heterogeneous formation under anisotropic *in-situ* stress. J. Nat. Gas Sci. Eng. 56, 455–471. https://doi.org/10.1016/j.jngse.2018.06.009.

Haimson, B., Fairhurst, C., 1967. Initiation and extension of hydraulic fractures in rocks. SPE J. 7 (03), 310–318. https://doi.org/10.2118/1710-PA.

He, J., Rui, Z., Ling, K., 2016. A new method to determi'e Biot's coefficients of Bakken samples. J. Nat. Gas. Sci. Eng. 35, 259–264. https://doi.org/10.1016/j.jngse.2016.08.061.

Hu, D.W., Zhou, H., Zhang, F., Shao, J.F., 2010. Evolution of poroelastic properties and permeability in damaged sandstone. Int. J. Rock Mech. Min. Sci. 47 (6), 962–973. https://doi.org/10.1016/j.ijrmms.2010.06.007.

Huang, J., Morris, J.P., Fu, P., Settgast, R.R., Sherman, C.S., Ryerson, F.J., 2019. Hydraulic-fracture-height growth under the combined influence of stress barriers and natural fractures. SPE J. 24 (01), 302–318. https://doi.org/10.2118/189861-PA.

Ishida, T., Chen, Q., Mizuta, Y., Roegiers, J.C., 2004. Influence of fluid viscosity on the hydraulic fracturing mechanism. J. Energy Resour. Technol. 126 (3), 190–200. https://doi.org/10.1115/1.1791651.

Jeffrey, R.G. & Settari, A. (1995). A comparison of hydraulic fracture field experiments, including mineback geometry data, with numerical fracture model simulations. In Proceedings of the *SPE Annual Technical Conference and Exhib*ition.10.2118/30508-MS.

Khalil, R., Emadi, H., 2020. An experimental investigation of cryogenic treatments effects on porosity, permeability, and mechanical properties of marcellus downhole core samples. J. Nat. Gas Sci. Eng. 81, 103422 https://doi.org/10.1016/j.jngse.2020.103422.

Knight, E.E., Rougier, E., Lei, Z., Euser, B., Chau, V., Boyce, S.H., Gao, K., Okubo, K., Froment, M., 2020. HOSS: an implementation of the combined finite-discrete element method. Comput. Part. Mech. 7 (5), 765–787. https://doi.org/10.1007/s40571-020-00349-y.

Kolawole, O., Ispas, I., 2020. Interaction between hydraulic fractures and natural fractures: current status and prospective directions. J. Pet. Explor. Prod. Technol. 10 (4), 1613–1634. https://doi.org/10.1007/s13202-019-00778-3.

Kresse, O., Weng, X., Gu, H., Wu, R., 2013. Numerical modeling of hydraulic fractures interaction in complex naturally fractured formations. Rock Mech. Rock Eng. 46, 555–568. https://doi.org/10.1007/s00603-012-0359-2.

Lander, R.H., Laubach, S.E., 2015. Insights into rates of fracture growth and sealing from a model for quartz cementation in fractured sandstones. GSA Bull. 127 (3–4), 516–538. https://doi.org/10.1130/B31092.1.

Le Calvez, J.H., Craven, M.E., Klem, R.C., Baihly, J.D., Bennett, L.A., Brook, K., 2007. Real-time microseismic monitoring of hydraulic fracture treatment: a tool to improve completion and reservoir management. Proceedings of the SPE Hdraulic Fracturing Technology Conference, Society of Petroleum Engineers. https://doi.org/10.2118/106159-MS.

Lecampion, B., Peirce, A., Detournay, E., Zhang, X., Chen, Z., Bunger, A., Detournay, C., Napier, J., Abbas, S., Garagash, D., and Cundall P. (2013). The impact of the near-tip logic on the accuracy and convergence rate of hydraulic fracture simulators compared to reference solutions. Proceedings of the *ISRM International Conference for Effective and Sustainable Hydraulic Fracturing*, Brisbane, Australia.

Lei, G., Dong, P.C., Mo, S.Y., Yang, S., Wu, Z.S., Cai, H., 2015. Calculation of full permeability tensor for fractured anisotropic media. J. Pet. Explor. Prod. Technol. 5, 167–176. https://doi.org/10.1007/s13202-014-0138-6.

Lei, Z., Rougier, E., Knight, E.E., Munjiza, A., 2014. A framework for grand scale parallelization of the combined finite discrete element method in 2d. Comput. Part. Mech. 1 (3), 307–319. https://doi.org/10.1007/s40571-014-0026-3.

Li, C., Caner, F.C., Chau, V.T., Bažant, Z.P., 2017. Spherocylindrical microplane constitutive model for shale and other anisotropic rocks. J. Mech. Phys. Solids 103, 155–178. https://doi.org/10.1016/j.jmps.2017.03.006.

Li, W.F., Frash, L.P. Carey, J.W., Welch, H.J., Meng, M., Nguyen, H., Viswanathan, H., Rougier, E., Lei, Z., Rahimi-Aghdam, S., & Bažant, Z.P. (2021a). Injection Parameters that Promote Branching of Hydraulic Cracks. *Geophys. Res. Lett.,*48(12):p.e2021GL093321. https://doi.org/10.1029/2021GL093321.

Li W.F., Lei Z., Chau V., Frash L.P., Carey J.W., Meng M., Rougier, E., Viswanathan H.S., Karra S., Nguyen H. & Bažant Z.P. (2021b). 3D Numerical Modeling of Hydraulic Fracture Branching. *55th US Rock Mechanics/Geomechanics Symposium*, Houston, Texas, USA.

Lichtner, P.C., Hammond, G.E., Lu, C., Karra, S., Bisht, G., Andre, B., Mills, R., Kumar, J., 2015. PFLOTRAN User manual: A massively Parallel Reactive Flow and Transport Model For Describing Surface and Subsurface Processes (No. LA-UR-15-20403). Los Alamos National Lab.(LANL), Los Alamos, NM, USA.

Liu, D., Lecampion, B., 2021. Propagation of a plane-strain hydraulic fracture accounting for a rough cohesive zone. J. Mech. Phys. Solids 149, 104322.

Manchanda, R., Shrivastava, K., Zheng, S., Sharma, M., 2020. A new mechanism for the formation of hydraulic fracture swarms. Proceedings of the SPE Hydraulic Fracturing Technology Conference and Exhibition, Woodlands, Texas. https://doi.org/10.2118/199725-MS.

Maxwell, S.C. & Cipolla, C.L. (2011). What does microseismicity tell us about hydraulic fracturing? In Proceedings of the SPE Annual Technical Conference and Exhibition, Society of Petroleum Engineers. 10.2118/146932-MS.

Mayerhofer, M.J., Stegent, N.A., Barth, J.O., & Ryan, K.M. (2011). Integrating fracture diagnostics and engineering data in the Marcellus shale. Proceedings of the SPE Annual Technical Conference and Exhibition, Denver, Colorado, USA. 10.2118/145463-MS.

Mokhtari, M., Tutuncu, A.N., 2015. Characterization of anisotropy in the permeability of organic-rich shales. J. Pet. Sci. Eng. 133, 496–506. https://doi.org/10.1016/j.petrol.2015.05.024.

Moukhtari, F.E., Lecampion, B., Zia, H., 2020. Planar hydraulic fracture growth perpendicular to the isotropy plane in a transversely isotropic material. J. Mech. Phys. Solids 137, 103878.

Munjiza, A.A., 2004. The Combined Finite-Discrete Element Method. John Wiley & Sons.

Olson, J.E., 2004. Predicting fracture swarms—The influence of subcritical crack growth and the crack-tip process zone on joint spacing in rock. In: Geological Society, 231. Special Publications, London, pp. 73–88. https://doi.org/10.1144/GSL.SP.2004.231.01.05.

Ortega, J.A., Ulm, F.J., Abousleiman, Y., 2007. The effect of the nanogranular nature of shale on their poroelastic behavior. Acta Geotech. 2 (3), 155–182. https://doi.org/10.1007/s11440-007-0038-8.

Pan, Z., Ma, Y., Connell, L.D., Down, D.I., Camilleri, M., 2015. Measuring anisotropic permeability using a cubic shale sample in a triaxial cell. J. Nat. Gas Sci. Eng. 26, 336–344. https://doi.org/10.1016/j.jngse.2015.05.036.

Rahimi-Aghdam, S., Chau, V.T., Lee, H., Nguyen, H., Li, W., Karra, S., Rougier, E., Viswanathan, H., Srinivasan, G., Bažant, Z.P., 2019. Branching of hydraulic cracks enabling permeability of gas or oil shale with closed natural fractures. Proc. Natl. Acad. Sci. U. S. A. 116 (5), 1532–1537. https://doi.org/10.1073/pnas.1818529116.

Renshaw, C.E., Pollard, D.D., 1995. An experimentally verified criterion for propagation across unbounded frictional interfaces in brittle, linear elastic materials. Int. J. Rock Mech. Min. Sci. Geomech. Abstr. 32 (03), 237–249. https://doi.org/10.1016/0148-9062(94)00037-4.

Kanin, E.A., Dontsov, E.V., Garagash, D.I., Osiptsov, A.A., 2020. A radial hydraulic fracture with pressure-dependent leak-off. J. Mech. Phys. Solids 143, 104062.

Shao, J.F., 1998. Poroelastic behaviour of brittle rock materials with anisotropic damage. Mech. Mater. 30 (1), 41–53. https://doi.org/10.1016/S0167-6636(98)00025-8.

Soeder, D.J., 1988. Porosity and permeability of eastern Devonian gas shale. SPE Form. Eval. 3 (01), 116–124. https://doi.org/10.2118/15213-PA.

Sun, Y., Chen, B., Edwards, M.G., Li, C., 2021. Investigation of hydraulic fracture branching in porous media with a hybrid finite element and peridynamic approach. Theor. Appl. Fract. Mech., 103133 https://doi.org/10.1016/j.tafmec.2021.103133.

Taleghani, A.D. (2010). Fracture re-initiation as a possible branching mechanism during hydraulic fracturing. In Proceedings of the 44th US Rock Mechanics Symposium and 5th US-Canada Rock Mechanics Symposium, Salt Lake City, Utah.

Tan, P., Jin, Y., Han, K., Hou, B., Chen, M., Guo, X., Gao, J., 2017. Analysis of hydraulic fracture initiation and vertical propagation behavior in laminated shale formation. Fuel 206, 482–493. https://doi.org/10.1016/j.fuel.2017.05.033.

Tan, X., Konietzky, H., Frühwirt, T., 2015. Experimental and numerical study on evolution of Biot's coefficient during failure process for brittle rocks. Rock Mech. Rock Eng. 48, 1289–1296. https://doi.org/10.1007/s00603-014-0618-5.

Tarahhom, F., Sepehrnoori, K., Marcondes, F., 2009. A novel approach to integrate dual porosity model and full permeability tensor representation in fractures. In: Proceedings of the SPE Reservoir Simulation Symposium. Woodlands, TX. https://doi.org/10.2118/119001-MS.

Valkó, P., Economides, M.J., 1995. Hydraulic Fracture Mechanics. Wiley, New York.

Warpinski, N.R., Teufel, L.W., 1987. Influence of geologic discontinuities on hydraulic fracture propagation. J. Pet. Technol. 39 (02), 209–220. https://doi.org/10.2118/13224-PA.

Welch, N.J., Carey, J.W., Frash, L.P., Hyman, J.D., Hicks, W., Meng, M., Li, W., Menefee, A., 2021. Effect of shear displacement and stress changes on fracture hydraulic aperture and flow anisotropy. Transp Porous Med. https://doi.org/10.1007/s11242-021-01708-w.

Weng, X., Kresse, O., Cohen, C., Wu, R., Gu, H., 2011. Modeling of hydraulic-fracture-network propagation in a naturally fractured formation. SPE Prod. Oper. 26 (04), 368–380. https://doi.org/10.2118/140253-PA.

Witherspoon, P.A., Wang, J.S., Iwai, K., Gale, J.E., 1980. Validity of cubic law for fluid flow in a deformable rock fracture. Water Resour. Res. 16 (6), 1016–1024. https://doi.org/10.1029/WR016i006p01016.

Wu, R., Germanovich, L.N., Hurt, R.S., 2009. Experimental and theoretical study of mixed-mode I+ III crack propagation and segmentation. North Carolina, Asheville.

Yoon, J.S., Zimmermann, G., Zang, A., 2015. Numerical investigation on stress shadowing in fluid injection-induced fracture propagation in naturally fractured geothermal reservoirs. Rock Mech. Rock Eng. 48 (4), 1439–1454. https://doi.org/10.1007/s00603-014-0695-5.

Zamirian, M., Aminian, K., Ameri, S., 2016. Measuring Marcellus shale petrophysical properties. Proceedings of theSPE Western Regional Meeting. Anchorage, Alaska.10.2118/180366-MS.

Zhang, Z., Peng, S., Ghassemi, A., Ge, X., 2016. Simulation of complex hydraulic fracture generation in reservoir stimulation. J. Pet. Sci. Eng. 146, 272–285.

Zoback, M.D., Rummel, F., Jung, R., Raleigh, C.B., 1977. Laboratory hydraulic fracturing experiments in intact and pre-fractured rock. Int. J. Rock Mech. Min. Sci. Geomech. Abstr. 14 (2), 49–58. https://doi.org/10.1016/0148-9062(77)90196-6.